

Analytic model of electron transport through and over non-linear barriers

Cite as: J. Appl. Phys. **127**, 235301 (2020); <https://doi.org/10.1063/5.0009759>

Submitted: 03 April 2020 . Accepted: 29 May 2020 . Published Online: 17 June 2020

 Kevin L. Jensen, Andrew Shabaev, Sam G. Lambrakos,  Daniel Finkenstadt, Nathan A. Moody, Amanda J. Neukirch, Sergei Tretiak, Donald A. Shiffler, and John J. Petillo



View Online



Export Citation



CrossMark

ARTICLES YOU MAY BE INTERESTED IN

[An extended moments model of quantum efficiency for metals and semiconductors](#)

Journal of Applied Physics **128**, 015301 (2020); <https://doi.org/10.1063/5.0011145>

[Harmonic generation at the nanoscale](#)

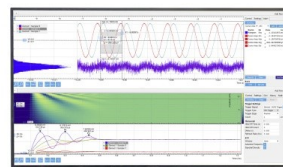
Journal of Applied Physics **127**, 230901 (2020); <https://doi.org/10.1063/5.0006093>

[Defects in Semiconductors](#)

Journal of Applied Physics **127**, 190401 (2020); <https://doi.org/10.1063/5.0012677>

Challenge us.

What are your needs for
periodic signal detection?



Zurich
Instruments




Analytic model of electron transport through and over non-linear barriers

Cite as: J. Appl. Phys. 127, 235301 (2020); doi: 10.1063/5.0009759

Submitted: 3 April 2020 · Accepted: 29 May 2020 ·

Published Online: 17 June 2020



Kevin L. Jensen,^{1,a)}  Andrew Shabaev,¹ Sam G. Lambrakos,¹ Daniel Finkenstadt,²  Nathan A. Moody,³
Amanda J. Neukirch,³ Sergei Tretiak,³ Donald A. Shiffler,⁴ and John J. Petillo⁵

AFFILIATIONS

¹Naval Research Laboratory, Washington, DC 20375, USA

²US Naval Academy, Annapolis, Maryland 21402, USA

³Los Alamos National Laboratory, Los Alamos, New Mexico 87545, USA

⁴Directed Energy Directorate, Air Force Research Laboratory, Albuquerque, New Mexico 87117, USA

⁵Center for Electromagnetics, DEOST, Leidos, Billerica, Massachusetts 01821, USA

^{a)}Author to whom correspondence should be addressed: kljensen@ieee.org

ABSTRACT

Tunneling barriers are an essential component of electron sources, sensors, detectors, and vacuum nanoelectronics and a pivotal factor in their performance, but the barriers themselves routinely depart from the analytic models used to model their behavior. A new formalism is developed to analytically and accurately model emission through and over barriers associated with depletion layers, nanotip barriers, and metal–insulator–metal (MIM) structures. The transmission probability for depletion layers and MIM and metal–oxide–semiconductor (MOS) barriers is accurately modeled as the electron energy exceeds the barrier height using approaches designed for rapid implementation demanded by simulation codes and extensible to general barriers. The models supersede conventional thermal and field models in depletion and MIM/MOS barrier studies. Thermal-field methods are used to treat the transmission probability and shape factor methods to treat the tunneling factor. Analytic formulas for current density are obtained. The methods ease device simulation and characterization of current–voltage relations for emerging technologically interesting barriers with better accuracy.

<https://doi.org/10.1063/5.0009759>

I. INTRODUCTION

Emerging technologies where efficient and rapidly modulated emission or tunneling is desired (and even conditions such as high field breakdown where it is problematic) are giving rise to circumstances where transport is not due primarily to thermal or field (tunneling) effects, but rather (i) entail a range of energies and distributions of electrons that can markedly differ from the presumptive Fermi–Dirac distribution on which the canonical equations are based or (ii) include processes that entail emission through barriers markedly different than those leading to the canonical equations particularly for thermal, field, and photoemission. These technologies include photo-enhanced thermionic emission,^{1,2} photoexcitation through layers and interfaces,^{3,4} barriers associated with coatings,⁵ nano-scale plasmonic junctions,⁶ photonic bandgap (PBG) devices and field effect transistors (FETs),^{7–9} nanoscale vacuum channel transistors and electronics,^{10–12} field emission

associated with multi-photon absorption from atomically small tips,^{13,14} voltage breakdown¹⁵ due to microparticles¹⁶ and micro-discharges,¹⁷ field emission and resonant tunneling effects in breakdown,^{18,19} generation of high power microwave devices and directed energy,^{20–22} Monte Carlo simulations of photoemission²³ and secondary emission,²⁴ emission from graphene,²⁵ space charge limited flow in the quantum regime²⁶ and for nanogaps,²⁷ and interfaces between photocathode²⁸ or detector materials and the metal contacts for x-ray detectors²⁹ or solar cells using perovskites.³⁰ In all such cases, device simulation requires accurate modeling of transport over a broad range of energies through and over the surface or contact barriers. The tunneling probability is required for energies below and beyond the height of the emission barrier and is dependent on the shape of the tunneling barrier itself, making use of the canonical equations at best problematic, and at worst inadequate, for describing the distribution of emitted or transported electrons.

It is often required that the emission models in simulation codes^{31–35} are compatible with the requirement for rapid algorithms when interactive effects due to space charge³⁶ and emittance growth³⁷ severely complicate simulation. As an example, in a generic simulation of a vacuum electronic anode–cathode (AK) gap for which space charge effects are integral (such as the simulation of Miram curves for thermal emitters³⁸), only a small fraction (~2%) of the emitted particles cross the space charge barrier and continue to the anode. The assumption of a Maxwell–Boltzmann (MB) distribution of those electrons is expeditious and enabling, but that *ad hoc* approximation is an *assumption*: given that the buildup of space charge before the barrier is heavily dependent on the distribution of electrons incident upon it and given that surface features (geometric and chemical roughness^{39–41}) have a pronounced impact on the distribution, the fine details of emission off the surface are increasingly important.

The treatment of the tunneling effect is historically one of the earliest and most impressive successes of quantum mechanics,⁴² explaining the emission of alpha particles from the nucleus^{43–45} or the emission of electrons from the surface of a metal subject to high fields^{46,47} observed by Millikan and Eyring.⁴⁸ Fowler and Nordheim’s (FN) model of field emission from metals considered a step barrier subject to a constant electric field \mathcal{E} [that is, a triangular barrier of the form $V(x) = V_o - q|\mathcal{E}|x \equiv V_o - Fx$], later amended to include an image charge contribution ($q^2/16\pi\epsilon_o x \equiv Q/x$) and used Sommerfeld and Bethe’s model of a metal. The methods were extended by Fowler to treat thermal and photoemission,^{49,50} ultimately giving rise to the “canonical” emission equations.⁵¹ The thermal emission equation due to Richardson and updated by Fowler^{49,52} was adapted by Bethe to treat the Schottky barrier between metals and semiconductors.^{53–55} The canonical equations are only qualitatively rather than quantitatively correct insofar as they presume a constant asymptotic field modified (at most) by an image charge close to the interface (the Schottky–Nordheim barrier), whereas depletion layers or barriers associated with nano-scale thickness films⁵⁶ and nanotip emitters⁵⁷ depart from those assumptions.

Accuracy is regained (and self-consistency enabled) through recourse to numerical methods that accurately solve Schrödinger’s equation for quantum effects^{58–61} and enable coupling with Poisson’s equation for charge distributions:^{6,62,63} the later effect is important when quantized levels exist in the depletion layer at the semiconductor–oxide interface and has consequences for the depth of the depletion layer.^{64–68} The recent work of Banerjee and Zhang,⁶³ who evaluate the tunneling current through an metal–insulator–metal (MIM)/metal–insulator–semiconductor (MIS)/metal–oxide–semiconductor (MOS) barrier and include self-consistent effects through a solution of a coupled Schrödinger equation and a Poisson equation, is notable: their study reflects how systematic and numerically intensive studies of MIM/MIS/MOS (and more general barriers) can be undertaken. These intensive approaches are superior for treating thin nanogaps, insulating films, and interfacial tunneling barriers, but they entail excessive computational efforts compared to the analytical models that device simulation, experimental characterization, and pedagogical models favor.

Depletion layer barriers at metal–semiconductor contacts^{68–74} are similar to emission barriers for highly curved surfaces^{75–79} or

nano-scale field emitters/emission sites^{27,80–83} or the inclusion of space charge effects in nano-gaps.⁶ Such barriers, modeled as in [Appendix B 1](#) when due to doping and [Appendix B 2](#) when due to the emitter curvature near prolate spheroidal tips, acquire a parabolic (concave up) nature away from the surface or interface. In contrast, thin barriers associated with MIM/MIS/MOS layers when the layers are thin acquire a parabolic (concave down) character for strong biases.⁸⁴ For specificity, a *quadratic barrier* (following Refs. 27 and 82) is taken to be of the form

$$\begin{aligned} V_\gamma(x) &= V_o - q|\mathcal{E}|x + \gamma x^2 - \frac{q^2}{16\pi K_s \epsilon_o x} \\ &\equiv V_o - Fx + \gamma x^2 - \frac{Q_s}{x}, \end{aligned} \quad (1)$$

with the γ -term accounting for the quadratic modification, where $\epsilon = K_s \epsilon_o$ is the dielectric constant in the medium of the barrier, and $Q_s = Q/K_s$ generalizes the image charge term $q^2/16\pi\epsilon_o \equiv Q$ [an electron in vacuum outside of a *semiconductor* experiences an image charge of $Q_s = Q(K_s - 1)/(K_s + 1)$,⁸⁵ but here, the electron is outside a *metal* and inside a material].

For narrative simplicity, henceforth, the MIM/MIS/MOS and depletion layer barriers are collectively referred to as a *MIM barrier*, as the barrier shape is the focus of the present work rather than consequences of depletion layers due to band bending, and therefore, the MIM barrier for a thin layer is most representative, even though the methodology applies to all. A MIM barrier introduces a contact replacing the vacuum anode, such that the presence of two closely spaced metal layers complicates the handling of the image charge terms. If the thickness of the insulator layer W is large, then a MIM barrier resembles

$$\begin{aligned} V_M(x) &= V_o - F_s x - V_m(x), \\ V_m(x) &\approx \frac{Q_s}{x} + \frac{Q_s}{W-x}, \end{aligned} \quad (2)$$

with $F_s = V_b/(K_s W)$ with V_b arising from the potential bias across the insulator and $V_m(x)$ replacing the standard image charge term $V_i(x) = Q_s/x$. For small x , to leading order, a term ($-Qx^2/W^3$) causes $V_M(x)$ to resemble a quadratic potential with a ($\gamma < 0$) term, but as the thickness decreases, an infinite series of images of image charges are required to maintain boundary conditions, giving rise to the forms of $V(x)$ encountered in [Sec. II C](#) and [Appendix B 3](#), where, as shall be seen, an analytic form good for all W is available. The full MIM barrier is shown in [Fig. 1\(b\)](#).

The inclusion of both an image term Q_s/x and a quadratic γx^2 or MIM term complicates subsequent derivations but is essential to accurately portray the tunneling *and* thermal physics and factored in the development of the shape factor method.⁸⁶ Because the barriers to be treated are several, the following nomenclature to refer to the types shown in [Fig. 1](#) is used: (i) a *linear barrier* corresponds to $\gamma = 0$ or $W \rightarrow \infty$ and is also referred to as a *Schottky–Nordheim* (SN) barrier, (ii) a *parabolic barrier* corresponds to $K_s = \infty$ (causing $Q_s = 0$) and is also referred to as a Schottky barrier, (iii) a *triangular barrier* corresponds to $K_s \rightarrow \infty$ and either $\gamma = 0$ or $W \rightarrow \infty$ (a finite W case will also be referred to as a trap-zoidal barrier), and (iv) a *MIM barrier* corresponds to finite K_s , a

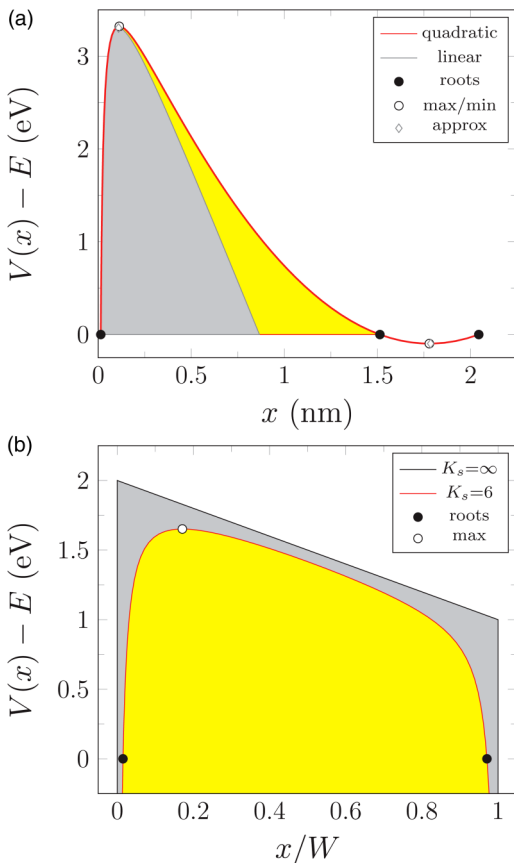


FIG. 1. Two kinds of non-linear potentials: (a) Quadratic barrier [Eq. (1)] for parameters $V_0 - E = 4.4$ eV, $K_s = 6$, $F = 5$ eV/nm, for quadratic ($\gamma = 1.4$ eV/nm², yellow fill) and linear ($\gamma = 0$, gray fill). (•) are the roots of $V(x) - E = 0$, and (◊) are the maximum x_o and minimum x_h locations with the gray ◊ marks at $\sqrt{Q_s/F}$ and $F/(2\gamma)$, respectively, that approximate their location. (b) MIM barrier for $V_0 - E = 2$ eV, $F = 0.5$ eV/nm, and $W = 2$ nm for the insulator ($K_s \rightarrow \infty$, gray fill) and the dielectric ($K_s = 6$, yellow fill).

distance between the contacts of W , and the inclusion of *all* image charge terms due to both contacts.

Consequently, the convention here is that linear, quadratic, and MIM barriers include image charge terms, whereas triangular, trapezoidal, and parabolic barriers do not. As a consequence, Schottky barriers are of the form $V(x) = V_0[1 - (x/w)]^2$ without the image charge term [e.g., Eq. (2.34) of Ref. 70]. The length w is referred to as the *depletion width*. The barriers are parameterized in Appendices B 1 and B 2.

The reliance on the canonical emission equations to treat quadratic and MIM barriers indicates the lack of an analytic transmission probability and particularly a closed form solution to the Gamow factor $\theta(E)$ upon which the commonly used JWKB transmission probability $D(E) = e^{-\theta(E)}$ depends. The reliance on numerical transfer matrix approximation methods^{58–61} to solve Schrödinger’s equation for more complex metal–semiconductor

and MIM barriers is often the only recourse, but although enabling high accuracy, doing so endures the loss of analytical convenience or computational expediency. Moreover, Fowler and Nordheim had assumed $\theta(E)$ was linear in energy (Appendix A): in fact, $\theta(E)$ is generally more strongly non-linear than it is for the SN barrier,⁶¹ and therefore, the use of Fowler–Nordheim parameterizations is even more problematic for non-linear barriers than they are for thermal-field emission evaluations. The shape factor method,^{27,61,86} developed as an intermediate technique to evaluating the Gamow factor $\theta(E)$ in pursuit of a general thermal-field equation,⁸⁷ has been used to treat non-linear barriers. An analytic approximation to $\theta(E)$ of sufficient accuracy results, from which methods for finding the modifications to a Fowler–Nordheim-like equation can then be developed but do *not* require a linear barrier or the resulting Schottky–Nordheim functions. The Gamow factor $\theta(E)$ is defined according to

$$\theta(E) \equiv 2 \int_{x_1}^{x_2} \sqrt{\frac{2m_n}{\hbar^2} [V(x') - E]} dx', \quad (3)$$

where m_n is the effective mass and the roots x_j are such that $V(x_j) - E = 0$. Introduce $\kappa(E)$ and $L(E)$ such that

$$\kappa(E) \equiv \left[\frac{2m_n}{\hbar^2} (V(x_o) - E) \right]^{1/2}, \quad (4)$$

$$L(E) \equiv x_2(E) - x_1(E). \quad (5)$$

For simplicity, the subscript on the effective electron mass m_n will be discontinued. The root index j is such that $x_j \leq x_{j+1}$ and $V(x_j) - E = 0$, whereas x_o is the smallest root of $\partial_x V(x_o) = 0$: for the linear barrier (Section II A) and MIM modification (Section II C), there is only one such x_o , but a quadratic barrier (Section II B) will have two. Thus, $\kappa(E)$ and $L(E)$ are seen to be the boundaries of the rectangle bounding the integrand of Eq. (3).

The shape factor $\sigma(y)$ is a dimensionless coefficient relating the integrand of Eq. (3) to the height $\kappa(E)$ and width $L(E)$ of the bounding rectangle enclosing it and is defined by

$$\theta(E) \equiv 2\sigma[y(E)]\kappa(E)L(E). \quad (6)$$

Although $\sigma(y)$ depends on the energy E of the tunneling particle, a dimensionless $y(E)$ that generalizes the argument of the Schottky–Nordheim functions $v(y)$ and $t(y)$ used by Murphy and Good⁸⁸ is the preferable argument, although the form of $y(E)$ will now depend on the nature of the potential and differ for the various non-linear barriers. Additionally, the shape factor is independent of the effective mass m_n in the tunneling region: the mass dependence resides in $\kappa(E)$ and, when different than the rest mass m , causes $\kappa \rightarrow \kappa\sqrt{m_n/m}$ and consequently the same dependence for θ . The present work will develop flexible and accurate methods of finding $\theta(E)$ using shape factor methods, and from it, linear approximations to $\theta(E)$ needed to enable analytic models of the current density past non-linear barriers.

The importance of the methods to be developed below is their requirement for providing accurate evaluations for the current

density in thermal-field conditions (when current due to tunneling is comparable to that due to thermal, or fly-over, emission) for which presently used methods are inadequate even for the SN barriers^{87,89} and, therefore, even more so for the non-linear barriers. Nevertheless, these methods also significantly modify current density estimates for common thermal or field emission conditions in conventional treatments, as shown using two representative examples based on the *ad hoc* barriers of Fig. 1 (the MIM barrier will magnify the inaccuracy). For thermal conditions, the primary source of error is the incorrect estimate of barrier height by an amount $\Delta\phi = 0.0173$ eV, equal to the difference in barrier heights of the “quadratic” and “linear” barriers. If J is the Richardson-Laue-Dushman (RLD) current for the non-linear barrier, and J_0 that for the linear barrier, then $J/J_0 \approx \exp(-\Delta\phi/k_B T)$, or 82.9% for $T = 1073$ K. For field conditions, the primary source of error is the incorrect estimate of $\theta(\mu)$. If J is the FN current for the non-linear barrier and J_0 that for the linear barrier, then $J/J_0 \approx \exp[\theta_0(\mu) - \theta(\mu)]$. Using $\theta(\mu)/\theta_0(\mu) \approx L(\mu)/L_0(\mu)$, it is found that $L(\mu)/L_0(\mu) \approx 133\%$ for $\mu = V_0/4$. The examples are pedagogical: MIM barriers and emission into vacuum for typical material parameters and operating conditions amplify the discrepancy.

II. SHAPE FACTOR METHOD

The shape factor method is developed for four types of barriers: (i) trapezoidal and triangular barriers, which are most commonly used in treating MIM as well as the FN barriers (Appendix A); (ii) Schottky–Nordheim (SN) barriers, which are the basis of the thermal, field, and photoemission canonical equations; (iii) quadratic barriers, which model depletion layers; and (iv) MIM barriers, which improve upon the trapezoidal barriers by including rounding effects due to image charges.

The triangular and trapezoidal barriers are the $K_s \rightarrow \infty$ limiting case of the SN and FN barriers and will be treated as such. When fields are high and/or insulator layers are thick, the SN and trapezoidal barriers are reasonable approximations for zero-temperature approximations. Consequently, the shape factor analysis will focus on three barrier types: the linear, quadratic, and MIM barriers. Finally, the notation and methods follow those introduced in shape factor method’s application to the SN barrier, as treated in Refs. 51 and 89. Because the extension to non-linear potentials engenders numerous new terms, a summary of the most important parameters is given in Table I.

A. Linear barrier

A linear barrier [Eq. (1) with $\gamma = 0$] results in the formalism of Murphy and Good (MG-FN)⁸⁸ and introduces elliptical integral functions $v(y)$ and $t(y)$, referred to as the Schottky–Nordheim functions by Forbes and Deane⁹⁰ (who also provide the most usable approximations to them), to account for image charge modifications to an otherwise triangular barrier. The use of the shape factor methodology^{27,61,86} gives the same results but without requiring $v(y)$ and $t(y)$. The method is synopsised here in a manner expedient to its generalization. The critical factor $y(E)$ will

TABLE I. Factors and parameter terms encountered in shape factor methods. μ and Φ (copper values are shown). See also Table II.

Symbol	Definition	Relation	Unit
$\theta(E)$	Gamow factor	Eq. (3)	...
$\kappa(E)$	$d\theta$ height	Eq. (4)	1/nm
$L(E)$	$d\theta$ width	Eq. (5)	1/nm
$\sigma[y(E)]$	$\theta(E)$ shape factor	Eq. (6)	1/nm
$\sigma_0[y(E)]$	Linear shape	Eq. (11)	1/nm
$\sigma_\gamma[y(E)]$	Quadratic shape	Eq. (18)	1/nm
$y(E)$	Shape ratio	Eq. (7)	...
y_{min}	Smallest y	Eq. (19)	...
$\sigma(y)$	Shape factor	Eq. (6)	...
μ	Chemical potential	7.0 (Cu)	eV
F	Field factor	$q \mathcal{E} $	eV/nm
T	Temperature	...	Kelvin
Q	Image term	$q^2/16\pi\epsilon_0$	eV nm
Q_s	Dielectric Q	Eq. (1)	eV/nm
Φ	Work function	4.5 (Cu)	eV
ϕ	Schottky lowered Φ	$\Phi - \sqrt{4QF}$	eV
$V_\gamma(x)$	Quadratic barrier	Eq. (13)	eV
$V_m(x)$	MIM barrier term	Eq. (29)	eV
V_0	Barrier height	$\mu + \Phi$	eV
G, H	MIM barrier factors	Eq. (34)	...
x_j	Roots of $V(x) - E$	Eq. (14)	nm
x_o	max $[V(x)]$ location	Eq. (15)	nm
x_h	min $[V(x)]$ location	Eq. (15)	nm
$R(a, b, c)$	θ -integral	Eq. (20)	...

always be taken to be defined by

$$y(E) \equiv \frac{V_0 - V(x_o)}{V_0 - E}, \quad (7)$$

where x_o is the location of the maximum of $V(x)$, which *does not change* with $V_0 - E$. It is seen that $y(E)$ corresponds to the ratio of how much the barrier is lowered through the application of a field compared to how far (in energy) the tunneling electron is below the maximum. For the standard image charge barrier $V(x) = V_0 - Fx - Q_s/x$, then $x_o = \sqrt{Q_s/F}$, and therefore, for $\gamma = 0$, $\sigma_\gamma(y) \rightarrow \sigma_0(y)$ and

$$y(E) = \frac{\sqrt{4Q_s F}}{V_0 - E}. \quad (8)$$

The y of the conventional Murphy–Good (MG) formulation is then seen to correspond to the special case $y(\mu) = \sqrt{4Q_s F}/\Phi$ when $V_0 = \mu + \Phi$ and figures prominently in standard accounts of the Fowler–Nordheim equation.^{51,88,90} The limit $y \rightarrow 0$ corresponds to a triangular barrier, and the limit $y \rightarrow 1$ describes an inverted parabolic barrier centered at $x_o = \sqrt{Q_s/F}$. In terms of x_o and x_j given by

$$x_j = \frac{V_0}{2F} \left[1 + (2j - 3)\sqrt{1 - y^2} \right], \quad (9)$$

then $\kappa(E)$ and $\sigma_0(y)$ are compactly recast as

$$\frac{\hbar^2 \kappa^2}{2m_n} = F \frac{(x_2 - x_o)(x_o - x_1)}{x_o}, \tag{10}$$

$$\sigma_0(y) = \int_{x_1}^{x_2} \left[\frac{x_o(x_2 - s)(s - x_1)}{s(x_2 - x_o)(x_o - x_1)} \right]^{1/2} \frac{ds}{L}, \tag{11}$$

where $L = x_2 - x_1$. A triangular barrier corresponds to $\sigma_0(0) = \sigma_\Delta = 2/3$, whereas a parabolic barrier corresponds to $\sigma_0(1) = \sigma_\Gamma = \pi/4$. Last, a good approximation to $\sigma_0(y)$ is⁸⁷

$$\sigma_0(y) \approx \sum_{j=0}^2 C_j \left(\frac{1-y}{1+y} \right)^j, \tag{12}$$

with the C_j given by $C_0 = \pi/4$, $C_1 = -0.092385$, and $C_2 = (2/3) - C_1 - C_0$.

B. Quadratic barrier

Non-linear potentials introduce more roots and modify the definition of x_o from being the location of the only maximum to now be the first maximum of $V(x)$. The generalization to the quadratic barrier is then to introduce another root x_3 , shift x_o away from $\sqrt{Q_s/F}$, and redefine y , after which modifications to $\sigma_\gamma(y)$ and κ are straightforward extensions of the linear barrier case.

Introducing $s \equiv x + (F/3\gamma)$, the quadratic potential of Eq. (1) can be rewritten as

$$\begin{aligned} V_\gamma(x) &= \frac{\gamma}{x} (s^3 - ps - r), \\ p &= \frac{F^2 - 3\gamma V_o}{3\gamma^2}, \\ r &= \frac{Q_s}{\gamma} - \frac{FV_o}{3\gamma^2} + \frac{2F^3}{27\gamma^3}, \end{aligned} \tag{13}$$

where the $1/x$ in the coefficient is for compactness as it does not affect the roots. The roots of the cubic $s^3 - ps - r$ are well known to be (compare Ref. 91)

$$\begin{aligned} s_k &= \sqrt{\frac{4}{3p}} \cos\left(\frac{\varphi}{3} - \frac{2\pi k}{3}\right), \\ \cos^2 \varphi &= \frac{27r^2}{4p^3} \end{aligned} \tag{14}$$

for $k = (0, 1, 2)$. The roots x_j are then given by $x_1 = s_2 + (F/3\gamma)$, $x_2 = s_1 + (F/3\gamma)$, and $x_3 = s_0 + (F/3\gamma)$. Alternately, the x_j can be found to good accuracy using a recursion relation [see Eq. (31) in Ref. 27]. The locations of the max/min points are found by recursion, with x_o being the smaller root of $\partial_x V(x) = 0$ and x_h being the

larger. The recursion relations are

$$\begin{aligned} x_o &\leftarrow \left[\frac{Q_s}{F - 2\gamma x_o} \right]^{1/2}, \\ x_h &\leftarrow \frac{Fx_h^2 - Q_s}{2\gamma x_h^2}, \end{aligned} \tag{15}$$

with $x_o \approx \sqrt{Q_s/F}$ and $x_h \approx (F/2\gamma)$ being the initial estimates. After five to eight iterations, reasonable convergence is achieved. Equation (7) for y becomes

$$y(E) = \frac{(F - \gamma x_o)x_o + (Q_s/x_o)}{V_o - E} \tag{16}$$

from which the $\gamma \rightarrow 0$ case of Eq. (8) is recovered appropriately because $x_o \rightarrow \sqrt{Q_s/F}$ in that limit.

The generalization of Eqs. (10) and (11) to non-linear barriers is now straightforward, with the quadratic barrier case given by

$$\frac{\hbar^2 \kappa^2}{2m_n} = \frac{\gamma}{x_o} \prod_{j=1}^3 (x_j - x_o), \tag{17}$$

$$\sigma_\gamma(y) = \int_{x_1}^{x_2} \left[\frac{x_o}{s} \prod_{j=1}^3 \left(\frac{x_j - s}{x_j - x_o} \right) \right]^{1/2} \frac{ds}{x_2 - x_1}, \tag{18}$$

where x_j and x_o must be obtained from Eqs. (14) and (15) first.

Two limiting cases are important. Analogous to Eq. (8), the limit of ($y \rightarrow 1$) corresponds to an inverted parabolic barrier for which x_1 and x_2 coalesce to x_o . Therefore, $\sigma_\gamma(1) \rightarrow \sigma_\Gamma = \pi/4$ as shown previously.^{27,87} The second limiting case is not the limit of ($y \rightarrow 0$) because that limit is excluded for non-zero γ by Eq. (8): rather, the smallest value of y , or y_{min} , is governed by that value of $V_o = V_{max}$ for which the roots x_2 and x_3 coalesce to x_h . Because x_o and x_h correspond to zeros of $\partial_x V(x) = 0$, they are independent of V_o . Consequently, $V_{max} = Fx_h - \gamma x_h^2 + (Q_s/x_h)$, and therefore, if the zero of energy is defined by $V(x_h) = 0$ (as shall be chosen below), then

$$\begin{aligned} y_{min} &= \frac{W - V(x_o)}{W} \\ &= \frac{x_h [Q_s + x_o^2(F - \gamma x_o)]}{x_o [Q_s + x_h^2(F - \gamma x_h)]}, \end{aligned} \tag{19}$$

which approaches $(4/27)\gamma F\sqrt{4QF}$ to leading order in γ , entailing that $y_{min} \rightarrow 0$ as $\gamma \rightarrow 0$ as per the discussion surrounding Eq. (8).

The limiting cases for $\sigma[y(E)]$ when $V_o - E$ approaches either $V_o - V(x_o)$ (maximum or $y = 1$) or $V(x_h) - E$ approaches 0 (minimum, $y = y_{min}$) are required. To proceed, define the function R by

$$R(a, b, c) \equiv \int_a^b \left\{ \frac{(x-a)(b-x)(c-x)}{x} \right\}^{1/2} dx, \tag{20}$$

where (a, b, c) will correspond to (x_1, x_2, x_3) , respectively, for which $R(a, b, c)$ becomes proportional to θ with the constant of

proportionality being $2\sqrt{2m\gamma}/h$ [the relationship between the roots x_j and the factors (V_o, F, Q_s, γ) is identified in Sec. IV A, specifically Eq. (63)]. For both limits, two of the roots will approach the same value: for the maximum (at x_o), then $a = b$, whereas for the minimum (at x_h), then $b = c$. Consider each in turn:

- Limiting case: $y \rightarrow y_{min}$: Near the apex of the barrier, the roots are such that $b = h - \delta$ and $c = h + \delta$, where h and δ are defined by these relations. Separate Eq. (20) into a dominant and a remainder part, or $R(a, b, c) = R(a, h, h) + \Delta R(h - \delta, h + \delta, c)$, where ΔR is defined by this relation. The integrand of ΔR is crudely trapezoidal, and because its contribution is small, it may be approximated by evaluating the integrand at the midpoint $h = (a + b)/2$ and multiplying it by the width of the integration region, or

$$\Delta R(a, b, c) \approx \frac{(c - b)(b - a)^2}{[\sqrt{b - a} + \sqrt{2c - b - a}]\sqrt{a + b}}. \quad (21)$$

In the limit that $\delta \rightarrow 0$, then $\Delta R \rightarrow (h - a)^{3/2}\delta/(h + a)^{1/2}$ and, therefore, vanishes. The dominant term $R(a, h, h)$ is, after a change of integration terms to $x = a \cosh^2 s$ and introducing $\cosh \chi = \sqrt{h/a}$, then

$$R(a, h, h) = 2ah \int_0^\chi \sinh^2 s \left[1 - \frac{a}{h} \sinh^2 s \right] ds. \quad (22)$$

The integrations are analytic, but because in general $h \gg a$, it can be shown

$$R(a, h, h) \approx \frac{h^2}{2} \left[1 - \frac{a}{h} \ln \left(\frac{4a}{h} \right) \right]. \quad (23)$$

The leading order approximation to $\kappa \propto \sqrt{V(x_o)/\gamma}$ and the approximation $x_o \approx \sqrt{Q/F} = [ah^2/(a + 2h)]^{1/2}$ are used to determine $\kappa \approx h[1 - 2\sqrt{2a/h}]^{1/2}$. The width L is simply $L = h - a$. As a result, in the limit $a/h \rightarrow 0$ and $\delta = 0$, then $R(0, h, h) = h^2/2$ and $\sigma_\gamma(y_{min}) = \sigma_\cup = 1/2 \equiv \sigma_\cup$. It is seen that the concave-up parabolic σ_\cup is a fourth constant shape factor (in addition to the rectangular σ_\square , triangular σ_Δ , and inverted parabolic σ_\cap cases²⁷) that describes barriers relevant to transport and emission.

- Limiting case: $y \rightarrow 1$: Analogous approximations occur near the apex of the barrier when $y(E) \lesssim 1$. In the (a, b, c) root notation of above, then the roots are such that $a = h - \delta$ and $b = h + \delta$, where again h and δ are defined by these relations. As a result,

$$R(a, b, c) = \int_{h-\delta}^{h+\delta} \left[\frac{(c-x)[\delta^2 - (x-h)^2]}{x} \right]^{1/2} dx. \quad (24)$$

Substituting $x = h + \delta \sin s$ and letting $(c - x)/x \approx (c - h)/h$, then

$$R(h - \delta, h + \delta, c) \approx \frac{\pi}{2} \delta^2 \left(\frac{c - h}{h} \right)^{1/2}. \quad (25)$$

Because $h = x_o$, then $\kappa L = [(h - a)(b - h)(c - h)/h]^{1/2}(b - a) = 2\delta^2 \sqrt{(c - h)/h}$, and therefore, $\sigma_\gamma(1) = \pi/4 = \sigma_\cap$ as observed above.

For a quadratic barrier, the third root x_3 past x_h is a means of evaluating $\theta(E)$ through the tunneling barrier, not a feature of the depletion barrier itself. Were it to exist, a local minimum or a well between the x_2 and x_3 roots would be associated with energy levels. While such wells may be related to surfaces with coatings,⁵ the widths of the energy levels are then related to the nature of the well,⁹² but this line of inquiry is not pursued in the present study.

The behavior of $\sigma_\gamma(y)$ will differ from $\sigma_0(y)$ because of the largeness of the base of the quadratic barrier in Fig. 1, which imposes a cutoff y_{min} when $V_o - E < V(x_h)$ and transmission ceases. For example, in the case of field emission, if $V(x_h)$ was above the conduction band minimum of the metal (the zero point of E), then the transmission probability $D(E)$ would vanish for $0 \leq E \leq V(x_h)$ because $L(E) \rightarrow \infty$, and therefore, $\sigma_\gamma(y)$ is comprehensible only for $y \geq y_{min}$. This creates a need to change the discussion of how $y(E)$ varies: with the introduction of K_s , a triangular barrier is properly and exactly recovered in the $K_s \rightarrow 1$ limit, rather than only approximately for F large for linear barriers in field emission; moreover, for parabolic depletion barriers of the kind in Appendix B 1, a fixed N_d is presumed. Consequently, K_s is a more useful parameter to vary such that $K_s \rightarrow 1$ removes the image charge contribution altogether ($Q_s \rightarrow 0$), and $K_s \rightarrow \infty$ recovers the metal image charge contribution ($Q_s \rightarrow Q$). Thus, variations in K_s will mimic the transition from triangular barriers to Schottky-Nordheim barriers in field emission. Several representative cases are considered in Fig. 2, where $\sigma_\gamma(y)$ is compared to $\sigma_0(y)$. Observe that scaling the x -axis by $y \rightarrow \tilde{y}$ defined by

$$\tilde{y} = \frac{y - y_{min}}{1 - y_{min}} \quad (26)$$

causes the $\sigma_\gamma(\tilde{y})$ and $\sigma_0(y)$ to overlap, as anticipated by a prior study,²⁷ except near $y \gtrsim y_{min}$ where $\sigma_\gamma(\tilde{y} = 0) = 1/2$ but $\sigma_0(y = 0) = 2/3$, a consequence of barriers of hyperbolic emitters, as in Appendix B 2, being more akin to depletion barriers in the presence of a field in the dielectric, as in Appendix B 1. As a result, the introduction of σ_\cup has not been needed until now, when shape factor methods are applied to quadratic barriers.

The realization that $\sigma_\gamma(y) \approx \sigma_0(\tilde{y})$ where $\tilde{y} \equiv (y - y_{min})/(1 - y_{min})$ is remarkable for two reasons. First, it allows usage to be made of the far more easily evaluated $\sigma_0(y)$ factor for $y > 0.1$, given the later's convenient representation by Eq. (12). Second, although $\sigma_\gamma(y)$ varies with energy E , it does so weakly so that the energy slope factor $\beta_F(E_m) = -\partial_E \theta(E_m)$ derived from the Schottky barrier Gamow factor of Eq. (16) is dominated by the variation of $\kappa(E)$ and $L(E)$.

C. MIM barrier

An analytically solvable shape factor results when the insulator is of finite thickness W and the barrier takes on a trapezoidal shape. When $Q_s \rightarrow 0$, then $y(E) \rightarrow 0$ as well, and it, therefore, ceases to be a parameter that monitors the barrier shape. Therefore, define $\lambda = WF/(V_o - E)$ such that for $\lambda \leq 1$ [for which

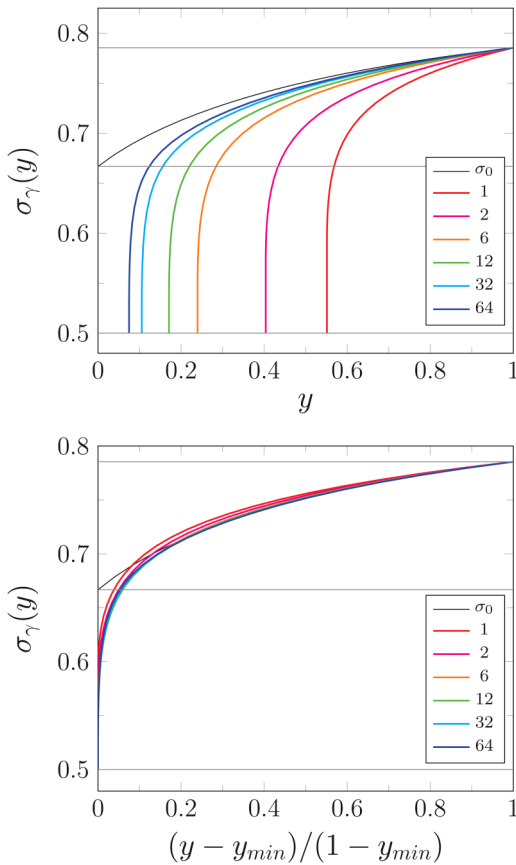


FIG. 2. (top) The shape factor $\sigma_\gamma(y)$ [Eq. (18)] with y and x_0 determined from Eqs. (16) and (15), respectively, with $F = 5$ eV/nm and $\gamma = 1.4$ eV/nm². (bottom) The same as above, but with $y \rightarrow (y - y_{min})/(1 - y_{min})$. The gray horizontal lines correspond to $\pi/4$, $2/3$, and $1/2$. The line marked $\sigma_0(y)$ is the linear barrier with $y_{min} = 0$ or Eq. (12). Lines are labeled by K_s .

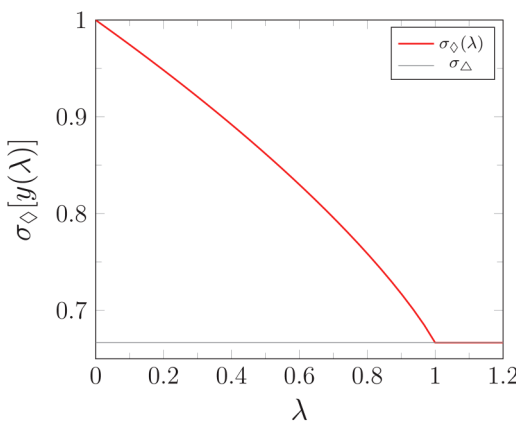


FIG. 3. Behavior of $\sigma_\diamond[y(\lambda)]$ as in Eq. (28). For $L(E) < W$, the triangular barrier $\sigma_\Delta = 2/3$ is recovered.

$L(E) = W]$, then

$$\lim_{K_s \rightarrow \infty} \sigma_m(y) \equiv \sigma_\diamond(\lambda) = \int_0^1 \sqrt{1 - \lambda s} ds, \quad (27)$$

whereas for $\lambda > 1$ [for which $L(E) < W$, that is, the barrier is triangular], then σ_Δ is recovered. Thus, the general trapezoidal barrier shape factor is

$$\sigma_\diamond(\lambda) = \begin{cases} \frac{2}{3\lambda} [1 - (1 - \lambda)^{3/2}] & (\lambda \leq 1), \\ \sigma_\Delta & (\lambda > 1) \end{cases} \quad (28)$$

so that at $\lambda = 1$, $\sigma_\diamond(1) = \sigma_\Delta = (2/3)$. The behavior is shown in Fig. 3.

Two metal contacts separated by a semiconductor with a finite dielectric constant K_s introduce an infinite number of image charges to describe the potential between the contacts. Beginning with the widely used formulation of Simmons⁸⁴ and introducing the dimensionless length term $s = x/W$, where W is the width of the insulator layer, the image charge contribution $V_i(x) = -Q_s/x \rightarrow -Q_s/Ws$ to the barrier in Eq. (2) is now replaced by $V_i(x) \rightarrow V_m(s)$,

$$V_m(s) = -\frac{2Q_s}{W} \left\{ \frac{1}{2s} + \sum_{j=1}^{\infty} \frac{s^2}{j(j^2 - s^2)} \right\}, \quad (29)$$

where $s = x/W$, which is equivalent to, but simplifies, Eq. (31) of Ref. 84, although it is noted that Simmons implies that the image charge potential contribution is $q^2/8\pi\epsilon_0 x = 2Q/x$, whereas the proper contribution is Q/x (or $q^2/4x$ in Gaussian units).^{61,93} Although Simmons characterized this equation as “extremely awkward” to work with due to its infinite series, an accurate and flexible approximation to it can be developed by utilizing Riemann’s zeta function defined by $\zeta(p) = \sum_{j=1}^{\infty} j^{-p}$. By Taylor expanding the $1/(j^2 - s^2)$ term and performing the j summation, we find

$$\sum_{j=1}^{\infty} \frac{1}{j(j^2 - s^2)} = \frac{1}{1 - s^2} + \sum_{k=0}^{\infty} [\zeta(2k + 3) - 1] s^{2k}. \quad (30)$$

Owing to the rapidity with which $\zeta(p)$ approaches 1 as p increases as per Eq. (C3), the summation over k can be truncated after only a few terms. Identifying $a = \zeta(3) - 1 = 0.202057$ and $b = \zeta(5) - 1 = 0.0369278$, the approximation

$$V_m(s) \approx -\frac{2Q_s}{W} \left\{ \frac{s^2}{1 - s^2} + \frac{1 + 2as^2 + 2bs^5}{2s} \right\} \quad (31)$$

is found and transformed into Eq. (B12) in Appendix B 3. By way of comparison, the approximate form suggested by Simmons [Eq. (33) of Ref. 84] is given by the corrected form $V_m(s) \approx -0.6931Q_s/[Ws(1 - s)]$ and shown as the blue line in Fig. 4.

The MIM shape factor $\sigma_m(y)$ with $y(E)$ as per Eq. (7) has more in common with the linear barriers of Sec. II A than the quadratic barriers of Sec. II B, as the underlying integrations

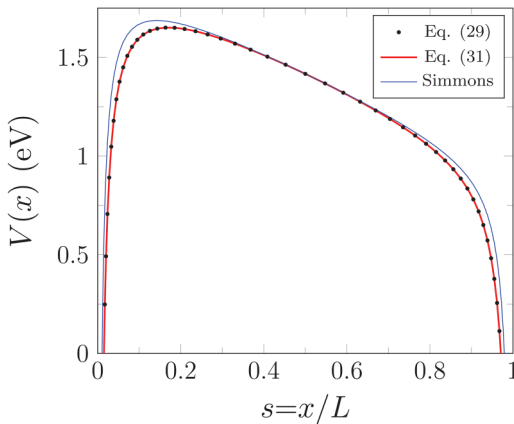


FIG. 4. For the same parameters as Fig. 1, evaluation of $V(x)$ using Eq. (29) (•) for the image charge contribution $V_i(x)$, to that using the approximate form [Eq. (31)] (red line). Also shown is $V(x)$ using the form $V_i(x) \approx -0.6931 Q_s / [Ls(1 - s)]$ based on Simmons⁸⁴ (blue line).

representing rounded trapezoids are closer in spirit to the rounded triangular (or Schottky–Nordheim) barriers than they are to the rounded parabolic (Schottky) barriers. Because of the complexity of Eq. (18), it may seem that $\sigma_m(y)$ requires numerical integration for its evaluation (or the comparatively crude approximations reviewed by Simmons⁸⁴), but good semi-analytic approximations are possible once the roots and maximum have been determined by the methods of Appendix B 3.

Methods of varying numerical complexities for the evaluation of $\sigma_m(y)$ based on Eq. (B12) are possible, but an attractive one makes use of the zeros of $V_m[s_j(E)] - E = 0$, which defines $s_j(E)$, and the location $s_o(E)$ of its maximum. A change of variables results in an integrand that is readily and rapidly evaluated by numerical means using, e.g., low order Gaussian quadrature, because the resulting integrand is well approximated by a polynomial. Define $Z(s) \equiv s(1 - s)[V_m(s) - E]$ as in Eq. (B17) and its derivative $Z'(s) = dZ/ds$ as in Eq. (B19). Assume a cubic form such that $Z(s) \approx A + Bs + Cs^2 + Ds^3$ with the coefficients determined by $Z(s)$ and $Z'(s)$ at the zeros $s_1(E)$ and $s_2(E)$ of the potential [that is, $V_m(s_j) - E = 0$] to find

$$\begin{bmatrix} 1 & s_1 & s_1^2 & s_1^3 \\ 1 & s_2 & s_2^2 & s_2^3 \\ 0 & 1 & 2s_1 & 3s_1^2 \\ 0 & 1 & 2s_2 & 3s_2^2 \end{bmatrix} \begin{pmatrix} A \\ B \\ C \\ D \end{pmatrix} = \begin{pmatrix} 0 \\ 0 \\ Z'(s_1) \\ Z'(s_2) \end{pmatrix}, \quad (32)$$

the inversion of which determines the coefficients exactly. However, an ansatz based on Eqs. (11) and (18) suggests

$$Z(s) \approx G(s - s_1)(s_2 - s)(H - s), \quad (33)$$

with G and H parameters to be determined by comparison to the cubic fit. The terms are dependent on E , but for simplicity, the dependence will be assumed rather than explicitly shown. It is

found that $G = D$ and $s_1 s_2 G H = -A$, from which

$$\begin{aligned} G &= \frac{Z'(s_2) + Z'(s_1)}{(s_2 - s_1)^2}, \\ H &= \frac{s_1 Z'(s_2) + s_2 Z'(s_1)}{Z'(s_2) + Z'(s_1)}. \end{aligned} \quad (34)$$

Asymptotic approximations are available in the $y \rightarrow 0$ (trapezoidal or triangular shape) and $y \rightarrow 1$ (inverted parabolic shape) limits. In the former, let $s_2 \rightarrow 1$ and $s_1 \rightarrow 0$ to find

$$\begin{aligned} G_0 &= FW - 0.04406 \left(\frac{Q_s}{2W} \right), \\ H_0 &= \frac{2(V_o W + Q_s)}{2FW^2 - 0.04406 Q_s}, \end{aligned} \quad (35)$$

where $4\zeta(5) + 4\zeta(3) - 9 = -0.04406$ [as per Eq. (31)]. In the latter, direct computation reveals $G_1 \approx G_0$ and $H_1 \approx 1$. A comparison of $Z(s)$ using the actual and approximate G and H is shown in Fig. 5, showing that using G_0 in general, and approximating H by H_0 for small y and 1 for a small $(1 - y)$, results in reasonable general choices. As a result, and given the polynomial-like nature of $Z(s)$ in Eq. (33), very rapid numerical algorithms are possible for the evaluation of $\sigma_m(y)$ making use of the analytical form of $Z(s)$ given in Eq. (33).

The shape factor $\sigma_m(y)$ for the MIM barrier can now be simplified. Using $Z(s)$, it follows:

$$\sigma_m(y) = \frac{1}{s_2 - s_1} \int_{s_1}^{s_2} \left[\frac{Z(s)s_o(1 - s_o)}{Z(s_o)s(1 - s)} \right]^{1/2} ds. \quad (36)$$

If Eq. (33) is used as an approximation for $Z(s)$, then the value of G is not required because $Z(s)$ and $Z(s_o)$ occur in ratios, and

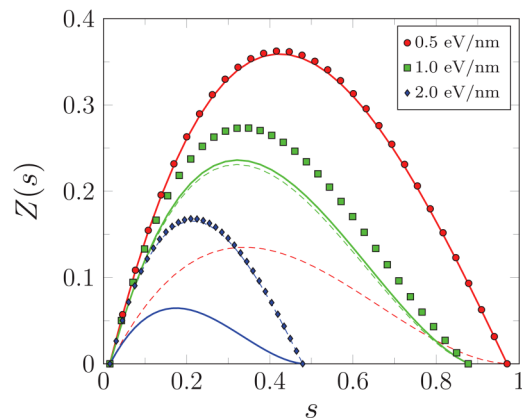


FIG. 5. Behavior of $Z(s)$ approximated by Eq. (33) using Eq. (34) (marks) compared to using $G \rightarrow G_0$ and $H \rightarrow H_0$ [Eq. (35), thick line] and using $G \rightarrow G_0$ and $H \rightarrow 1$ (dashed line) for the parameters $V_o - E = 2$ eV and $K_s = 6$, with $y(E) = [V_o - V(x_o)] / (V_o - E)$. The lines are labeled by F .

therefore, the approximate constancy of G allows for its neglect. Making the replacement $s = s_a + \Delta \sin \theta$, where $s_a = (s_2 + s_1)/2$, $\Delta = (s_2 - s_1)/2$, and $p = (s_a - s_o)/\Delta$, then

$$\sigma_m(y) \equiv C_\sigma \int_{-\pi/2}^{\pi/2} f_\sigma(\theta) \cos^2 \theta d\theta, \quad (37)$$

where the factors C_σ and $f_\sigma(\theta)$ are defined by

$$C_\sigma = \frac{1}{2} \left[\frac{(s_a + p\Delta)(1 - s_a - p\Delta)}{(1 - p^2)(H - s_a - p\Delta)} \right]^{1/2}, \quad (38)$$

$$f_\sigma(\theta) = \left[\frac{(H - s_a - \Delta \sin \theta)}{(s_a + \Delta \sin \theta)(1 - s_a - \Delta \sin \theta)} \right]^{1/2}.$$

The integrand of Eq. (37) is polynomial-like and vanishes at the limits of integration, allowing for its rapid evaluation by numerical means, e.g., using Gaussian quadrature or a summation based on Simpson's rule. Identifying its asymptotic limits is useful for identifying under what conditions the shape factor is triangular-like (σ_Δ) or parabola-like (σ_\cap):

1. The triangular limit ($y \rightarrow 0$) occurs for $4FQ_s \ll V_o^2$ (that is, small F and/or large K_s). Under such conditions, $\Delta \approx 1/2$ and $s_a \approx 1/2$, leading to a behavior of f_σ that mimics $f_\sigma(\sin \theta) \sim f_\sigma(0)/\cos(\theta)$ near the origin, leading to

$$\sigma_m(y) \approx 2C_\sigma f_\sigma(0) \sim \left[\frac{2H - 1}{2H - 2s_o} \right]^{1/2}, \quad (39)$$

where the approximation on the right-hand side is the limit of $\Delta \rightarrow 1/2$ and $s_a \rightarrow 1/2$. Using the $Q_s \rightarrow 0$ limit of Eq. (35), then $\sigma_m(y) \approx (1 - \lambda/2)^{1/2}$ and has the same small λ limit as the triangular part of Eq. (28).

2. The parabolic limit ($y \rightarrow 1$) occurs for $4FQ_s \approx V_o^2$ (that is, large F and/or small K_s), allowing for the approximation $f_\sigma(\sin \theta) \approx f_\sigma(0)$ (because $\cos^2 \theta$ is an even function, the linear dependence of $f_\sigma(\theta)$ on $\sin \theta$ does not survive), giving

$$\sigma_m(y) \approx \frac{\pi}{2} C_\sigma f_\sigma(0) \sim \frac{\pi}{4}, \quad (40)$$

where the right-hand side is the limit of $s_a \rightarrow s_o$ as $y \rightarrow 1$, recovering $\sigma_m(1) \approx \sigma_\cap = \pi/4$, as encountered in the discussion of Eq. (25), because the barrier is parabolic.

A comparison of $\sigma_m(y)$ as evaluated using Eq. (37) is shown in Fig. 6, compared to the limiting values given by Eqs. (39) and (40) (lines). Also shown is an albeit crude but analytic approximation based on Eq. (28) for $\lambda(E) \leq 1$ and the approximate linearity of $\sigma_m(y)$ for $\lambda(E) > 1$, given by

$$\sigma_\lambda(y) \equiv \begin{cases} \frac{2}{3\lambda} \left[1 - (1 - \lambda)^{3/2} \right] & (\lambda \leq 1), \\ \frac{2}{3} + \left(\frac{\pi - 2}{3} \right) \left[\frac{y - y_1}{1 - y_1} \right] & (\lambda > 1), \end{cases} \quad (41)$$

where $y_1 = (V_o - V(x_o))/WF$ [that is, the value of $y(E)$ when $\lambda = 1$ or $\sigma_\lambda(y_1) = 2/3$]. The approximation is an *ad hoc* means to

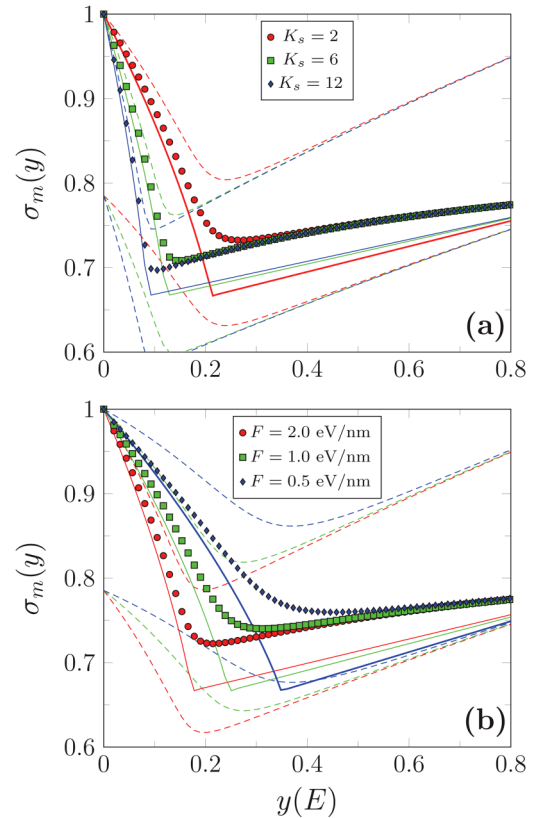


FIG. 6. Evaluation of $\sigma_m(y)$ [Eq. (37)]. (a) Using the parameters $W = 2$ nm, $F = 4$ eV/nm, $L = 2$ nm, with K_s as shown. Dashed lines correspond to $2C_\sigma f_\sigma(0)$ [Eq. (39)] and $(\pi/2)C_\sigma f_\sigma(0)$ [Eq. (40)]. Solid lines correspond to the analytic $\sigma_\lambda(y)$ of Eq. (41). (b) Same as (a) but now using $K_s = 6$ and $F = (0.5, 1.0, 2.0)$ eV/nm as shown. See also Fig. 8.

take into account the transition of the barrier shape from a triangular (σ_Δ) to an inverted parabola (σ_\cap) as $y \rightarrow 1$ on a path almost linear in y for $\lambda > 1$. Its accuracy is dependent upon how closely $\sigma_m(y_1)$ approaches $2/3$. The approximation is useful precisely because it is *completely analytic* and relies on only the parameters (V_o, F, W, K_s) and the energy E at which $y(E)$ is considered. Its efficacy is analyzed in Sec. IV B.

III. GENERAL THERMAL-FIELD METHODS

A brief review of methods^{60,61,94} leading to the general thermal-field (GTF) current density^{51,87} is given to prepare the generalization of J_{GTF} , applicable as is for Schottky barriers, to MIM structures. As with the shape factors, the notation follows Refs. 51 and 89, with terms given in Table II.

A. Current density

A statistical model of the current density J specifies current past a barrier as the product of the charge of the carrier q , the

TABLE II. Factors and parameter terms encountered in the GTF equations. See also Table I.

Symbol	Definition	Relation	Unit
$D(E)$	Transmission probability	Eq. (48)	...
$f(E)$	Supply function	Eq. (44)	1/nm ³
J_S	Current density	Eq. (45)	A/cm ²
J_{GTF}	Thermal-field J	Eq. (51)	A/cm ²
β_T	Thermal slope factor	$1/k_B T$	1/eV
β_F	Field slope factor	Eq. (53)	1/eV
$n(F, T)$	Energy slope ratio	β_T/β_F	...
$s(F, T)$	θ -expansion factor	Eq. (51)	...
E_m	max $[dJ(E)]$ location	Eq. (50)	eV
$N(n, s)$	dJ integral (linear θ)	Eq. (52)	...
$\Sigma(x)$	$N(n, s)$ function	Eq. (C2)	...

density ρ of the gas of particles, and the average velocity of the particles $\langle v_z \rangle$. The relevant distribution function from which ρ and $\langle v_z \rangle$ are evaluated is that of the particles that have successfully moved past the barrier by tunneling or fly-over and, therefore, goes as a tunneling probability $D(k_z)$ and a supply function $f(k_z)$, and therefore,

$$J_z = \frac{qg}{2\pi} \int \frac{\hbar k_z}{m} D(k_z) f(k_z) dk_z, \quad (42)$$

where a factor of $g = 2$ in the numerator of the coefficient accounts for electron spin. The probability of emission is

$$D(k_z) \equiv \frac{j_{trans}}{j_{inc}}, \quad (43)$$

$$j_k \equiv \frac{\hbar}{2mi} \left(\psi_k^\dagger \partial_z \psi_k - \psi_k \partial_z \psi_k^\dagger \right),$$

where *inc* and *trans* refer to the incident (left) and transmitted (right) wave functions ψ_k , respectively. The supply function is obtained from the Fermi-Dirac distribution $f_{FD}(E_{tot})$ and $E_{tot} = \hbar^2(k_z^2 + k_\perp^2)/2m$, where k_z is the *normal* component into the surface barrier and k_\perp the *transverse* component that is perpendicular to k_z , by integrating over the transverse or \vec{k}_\perp components, giving

$$f(E_z) = \frac{mk_B T}{\pi \hbar^2} \ln [1 + e^{\beta_T(\mu - E_z)}], \quad (44)$$

where the *thermal energy slope factor* $\beta_T \equiv 1/k_B T$. As the components are now descriptive of one-dimensional transmission along the \hat{z} -direction, it is common to (i) transform the integrals to normal energy E_z by using $k_z = \sqrt{2mE_z}/\hbar$ and (ii) discontinue usage of the z -subscript, resulting in, for Schottky and Schottky-Nordheim barriers, the current density given by

$$J_S = \frac{q}{2\pi \hbar} \int_0^\infty D(E) f(E) dE. \quad (45)$$

Such an equation presupposes no incident current from the right boundary, contrary to what occurs in an interface or MIM structure. An intuitive generalization to Eq. (45) is then to introduce a supply function for the right boundary, resulting in the Tsu-Esaki formula^{95,96} (also known as the Landauer formula) for the current density given by

$$J_M = \frac{q}{2\pi \hbar} \int_0^\infty D(E) [f(E) - f(E + V_b)] dE \quad (46)$$

for MIM and interface barriers [compare Eq. (7) of Ref. 84], where the right-hand side of the barrier is held at a lower value V_b . Under conditions where the Fermi level μ is negative [e.g., semiconductors with weak to moderate doping levels ($\leq 10^{18}$ cm⁻³)], then the Maxwell-Boltzmann approximation to Eq. (44) is useful, resulting in a relation for thermal emission-dominated conditions (that is, when tunneling is not significant) given by

$$f(E) - f(E + V_b) \approx f(E)(1 - e^{-\beta_T V_b}). \quad (47)$$

At low temperatures, or when tunneling is significant, subtracting the left and right directed currents results in greater complexity as considered by Simmons and for which new theory is developed below.

The development of the GTF equation requires further approximation to the Kemble form of the transmission probability, given by^{5,88,97}

$$D(E) = \frac{1}{1 + e^{\theta(E)}}, \quad (48)$$

where the Gamow factor $\theta(E)$ is approximated by its tangent line,

$$\theta(E) \approx \theta(E_m) - \beta_F(E_m)(E_m - E), \quad (49)$$

where E_m is the location of the maximum of the $D(E)f(E)$ integrand of Eq. (45), that is,

$$\left. \frac{d}{dE} [D(E)f(E)] \right|_{E=E_m} = 0. \quad (50)$$

$J_S(F, T)$ is approximated by the general thermal-field approximation,

$$J_{GTF}(F, T) = A_{RLD} T^2 N(n, s),$$

$$n(F, T) = \frac{\beta_T}{\beta_F(E_m)}, \quad (51)$$

$$s(F, T) = \theta(E_m) - \beta_F(E_m)(\mu - E_m),$$

where A_{RLD} is as in Appendix A, and the function $N(n, s)$ is given by

$$N(n, s) = n \int_{-\infty}^\infty \frac{\ln [1 + e^{n(x-s)}]}{1 + e^x} dx \quad (52)$$

and admits of further approximations that separate into thermal-dominated and field-dominated components described in Appendix C. Approximations to $N(n, s)$ suitable for numerical work are given by Eq. (C1). In the integral form of Eq. (52), the numerator of the integrand arises from the supply function and the denominator from the Kemble approximation using the linear Gamow factor of Eq. (49). Finding E_m requires additional methods previously developed.⁸⁹ The impact of the non-linear barriers [that is, $V_\gamma(x)$ and $V_M(x)$] on $J(F, T)$, therefore, manifests itself in the changes to $\theta(E_m)$ and $\beta_F(E_m)$ of Eq. (51): the current through a depletion layer and an MIM barrier will be modified in the same way that $J_{GTF}(F, T)$ replaces the canonical Fowler–Nordheim and Richardson–Laue–Dushman equations of field and thermal emission, respectively.

B. Linear barrier energy slope factor

The quadratic and MIM barriers will undermine the linear approximation of Eq. (49), as the non-linearity of $\theta(E)$ is more pronounced for the non-linear barriers, in three ways: (i) compared to the Bethe thermal emission or the Schottky emission model, the barrier height is raised for the depletion barrier and lowered for the MIM barrier; (ii) compared to the Fowler–Nordheim tunneling model, the barrier height and tunneling width at the Fermi level are both increased for the depletion barrier and reduced for the MIM barrier; and (iii) in the general thermal-field model, both the aforementioned effects result in changes to $\theta(E_m)$ [and, therefore, $s(F, T)$] and $\beta_F(E_m)$ [and, therefore, $n(F, T)$]. The complications in the thermal-field (TF) $\theta(E)$ due to its non-linearity have already been encountered, and successfully addressed, for the standard linear barrier model of Eq. (1) culminating in Eq. (52). What is important in the present treatment is the determination of E_m and $\beta_F(E) \equiv -\partial_E \theta(E)$, which requires having to consider both Eq. (3) for $\theta(E)$ and its derivative $\beta_F(E) = -\partial_E \theta(E)$. As a matter of computational expediency, this is undesirable, as requiring numerical integrations in emission models results in an excessive computational burden in both simulations and beam optics codes. An approximate solution is suggested by the shape factor methods. Observe that

$$\beta_F(E) = -\sigma(y)\partial_E[2\kappa L] - 2\kappa L\partial_E\sigma(y). \quad (53)$$

An approximate method based on the weak variation of $\sigma[y(E)]$ compared to that of $2\kappa(E)L(E)$ is computationally expedient, as the later can be determined directly from Eqs. (4) and (5) without the need for integration and the former is well approximated by Eq. (12) for $y(E)$ given by Eq. (7). Write Eq. (53) as

$$\begin{aligned} \beta_F(E) &= -2\sigma(y)\partial_E(\kappa L) \left\{ 1 + \frac{\partial_E \ln[\sigma(y)]}{\partial_E[\ln(\kappa L)]} \right\} \\ &\equiv \beta_F^0(E)[1 - R_\beta(y)], \end{aligned} \quad (54)$$

where $\beta_F^0(E)$ is the *constant shape factor* approximation to $\beta_F(E)$ and $R_\beta(y)$ is expected to be small. For the shape factors of Sec. II A,

Eqs. (9) and (10) give

$$\kappa L = \frac{4}{\hbar} \left(\frac{m^2 Q_s^3}{F} \right)^{1/4} \left[\frac{(1-y)(1-y^2)}{y^3} \right]^{1/2}, \quad (55)$$

where the form of $\sigma_0(y)$ can be obtained from Eq. (12), and then it is found that

$$\beta_F^0(E) = \frac{2}{\hbar} \left(\frac{m^2 Q}{F^3} \right)^{1/4} \frac{(y+3)}{\sqrt{y(1+y)}} \sigma_0(y), \quad (56)$$

$$R_\beta(y) = \frac{2y(1-y^2)}{y+3} \partial_y[\ln(\sigma_0(y))], \quad (57)$$

which is equivalent to Eq. (28) of Ref. 87. By taking derivatives of logarithms, the constant coefficients of $\sqrt{2m}/\hbar$ that accompany κL do not appear in R_β . Invoking Eq. (8) gives as a reasonable approximation

$$R_\beta(y) \approx 0.1865 \frac{y(1-y)(y+3.655)}{(y+0.5985)(y+1.308)(y+3)} \quad (58)$$

for which the absolute value is maximum at $R_\beta(0.3107) = 0.03251$. Therefore, a constant- σ approximation, in which $\beta_F(E) \approx \beta_F^0(E)$, may be adequate for numerical work, even though the inclusion of $R_\beta(y)$ is not difficult, as it allows for a reasonably accurate determination of E_m in a straightforward manner. Such an approximation, however, will not be used in the analyses below.

C. Nonlinear barrier energy slope factor

A similar expectation arises for $\sigma_\gamma(y)$ and $\sigma_m(y)$ [e.g., the discussion attending Eq. (26)] but must be demonstrated. To do so, rewrite Eq. (53) as

$$-\frac{\beta_F(E)}{\theta(E)} = \partial_E \ln\{\sigma[y(E)]\} + \partial_E \ln[\kappa(E)L(E)], \quad (59)$$

where the ratio of the first and second terms is equivalent to $-R_\beta(y)$ in Eq. (58). Evaluating the integrals defining $\sigma(y)$ numerically, and using finite difference approximations for the derivatives with respect to E , the comparison is shown in Fig. 7 for several representative parameters ($V_o = 4$ eV, $\gamma = 0.001$ eV/nm², $0 \leq E_j \leq V_o - \sqrt{4Q_s F}$ for $N = 80$ points). The choice of such parameters remains comparable to Fig. 1: if $L \rightarrow \alpha L$, $F \rightarrow \alpha F$, $Q_s \rightarrow Q_s/\alpha$, and $\gamma \rightarrow \gamma\alpha^2$, then the leading order behavior of the factors $V(x_o) \approx V_o - \sqrt{4Q_s F}$, $s_o \approx \sqrt{Q_s/FL^2}$, and $s_h \approx F/2\gamma L$ do not noticeably change, and therefore, $\sigma(y)$ and κL do not noticeably change, meaning that changing F by a factor of 1/10 suggests changing γ by a factor of 1/100. Except near the base of the barrier where $y(E)$ is small, the relative smallness of $-R_\beta(y)$ demonstrates that the constant- σ approximation is reasonable: for the parameters of Fig. 7, the minimum value of y is 0.0458–0.1122. Numerical

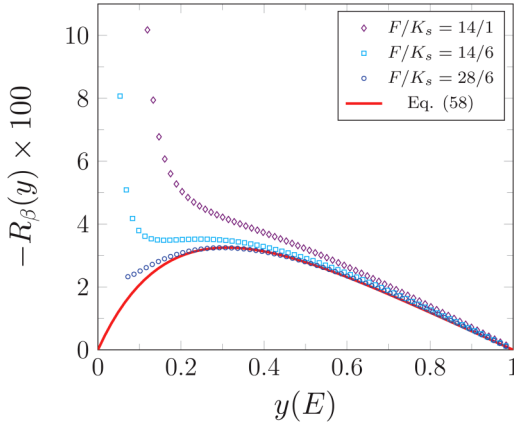


FIG. 7. Evaluation of $-R_\beta(y) = \partial_E \ln(\sigma_\gamma) / \partial_E \ln(\kappa L)$. The legend (F/K_s) indicates values of $100 \times F$ (with F in units of eV/nm) and K_s . For numerical evaluation, $V_o = 4$ eV and $\gamma = 0.001$ eV/nm². $\sigma_\gamma(y)$ integrations and derivatives with respect to E are numerically performed.

derivatives for a general function $f(E)$ are evaluated according to

$$\frac{f(E_j) - f(E_{j-1})}{E_j - E_{j-1}} = \frac{f_j - f_{j-1}}{E_j - E_{j-1}} \equiv f'_{j-1/2}, \quad (60)$$

with f corresponding to $\ln \sigma(y)$ or $\ln(\kappa L)$ here with the consequence that small departures from the analytic result of Eq. (58) are visible near $y \approx 1$.

The approximate adequacy of the constant- σ approximation entails that $\beta_F^o(E)$ may be used in place of $\beta_F(E)$ for energies near the middle of the quadratic barrier (or higher) and certainly for emission in the thermal-field regime. As the current density is rapidly suppressed for smaller energy [greater $V_o - E$ and, therefore, smaller $y(E)$], an advantage to simulation and evaluation becomes apparent due to the availability of reasonable analytic approximations to $\sigma_\gamma(y)$, thereby avoiding numerical integration compared to the simple function calls required to evaluate $\kappa(E)$ and $L(E)$, as they depend only on the values of (x_o, x_h) (maximum/minimum location) and $x_{1,2}$ (root location), are the largest contribution to $\beta_F(E)$, and can be interpolated to intermediate values of E with ease.

The analysis is now repeated for the MIM barrier $\sigma_m(y)$ factor. As before, finding what conditions $\beta_F^o(E)$ is a reasonable approximation to $\beta_F(E)$ requires comparing $d \ln(\sigma(y))/dE$ to $d \ln(\kappa L)/dE$. Approximate the derivatives numerically using finite difference methods. For MIM barriers, two limiting cases exist, the trapezoidal case where $L(E) = W$ and the triangular case where $L(E) = (V_o - E)/F$. They result in the $K_s \rightarrow \infty$ limiting cases of

$$\lim_{K_s \rightarrow \infty} \kappa(E)L(E) = \frac{\sqrt{2mFW^3}}{\hbar} \times \begin{cases} \lambda^{-3/2} & (\lambda \leq 1), \\ \lambda^{-1/2} & (\lambda > 1), \end{cases} \quad (61)$$

where $\lambda(E) = FW/(V_o - E)$. Consequently, $d \ln(\kappa L)/dE$ is compared to the limiting cases of $-(3/2)d \ln(\lambda)/dE$ and

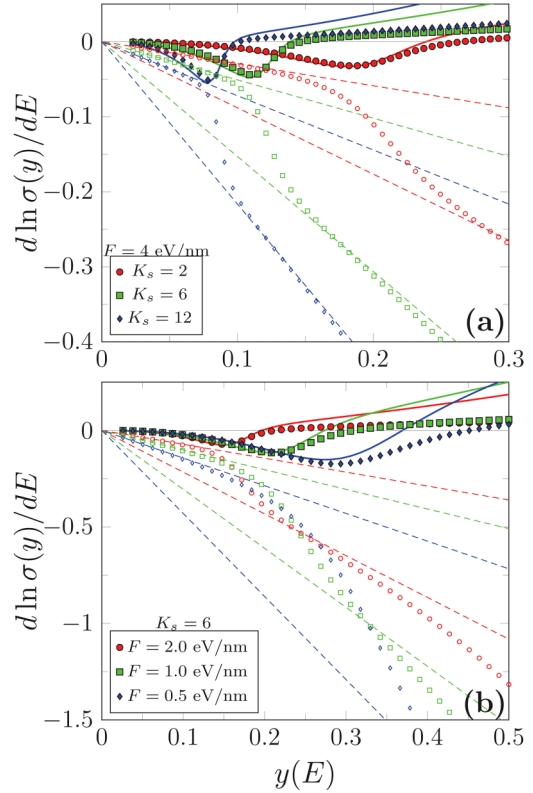


FIG. 8. Evaluation of $d \ln(\sigma)/dE$ for $\sigma(y)$ for the conditions of Fig. 6, where symbols (\circ , \square , \diamond) use $\sigma_m(y)$ of Eq. (36) and the thick solid lines use $2C_{\sigma}f_\sigma(0)$ of Eq. (39). Also shown are the limiting cases $d \ln(\kappa L)/dE$ when κL is given by Eq. (61) (dashed lines). (a) Variation with K_s . (b) Variation with F .

$-(1/2)d \ln(\lambda)/dE$, the four cases being shown in Fig. 8, demonstrating that using $\sigma(y) \approx 2C_{\sigma}f_\sigma(0)$ is good for small y , and that for larger y , the growth of $\kappa(E)L(E)$ diminishes its relative importance.

The common use of the Fowler–Nordheim equation of Appendix A, even for potentials that are demonstrably non-linear, however, owes much to the comparative simplicity of Eq. (A5) [or Eq. (A7) if the image charge contribution is included]. The requirement to obtain x_1, x_2, x_o , and x_h , even by approximate means, so as to use Eq. (36) [or Eqs. (39) and (40)] for the approximation of $\beta_F(E)$ may, therefore, be an impediment for the adoption of shape factor methods in simulations of MIM barriers. Therefore, consider the purely analytic and easily evaluated $\sigma_\lambda(y)$ of Eq. (41) as a heuristic alternate. Its performance for common values of $K_s = 6$ at relatively large and small fields of $F = 0.5$ and 4 eV/nm, compared to using $\sigma_m(y)$ [Eq. (36)] or its approximation by Eq. (39), is shown in Fig. 9. It is seen that for small y , where $d \ln(\kappa L)/dE$ is comparable to $d \ln(\sigma(y))/dE$, the approximation is good. Conversely, when y is closer to unity, then some conditions allow the approximation $\sigma_\lambda(y)$ to be good, but the comparative largeness of $d \ln(\kappa L)/dE$ signifies that even in this regime, the impact on $\beta_F(E)$ is the (as previously observed) marginal.

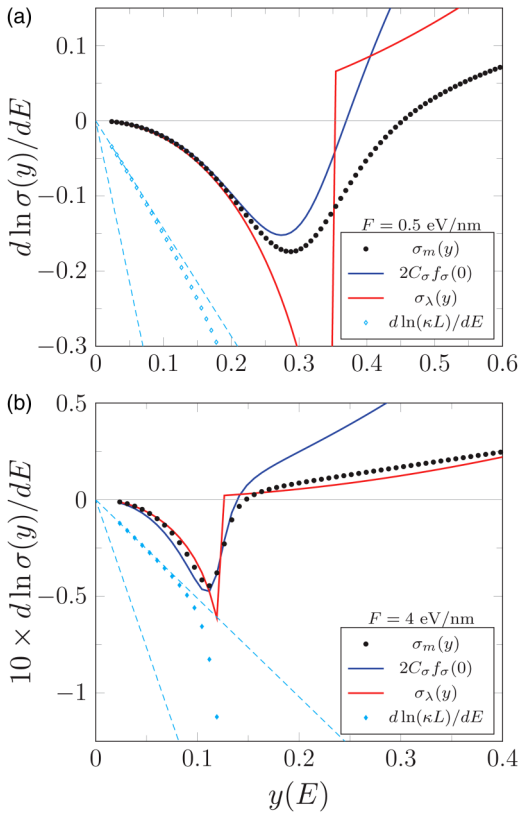


FIG. 9. Evaluation of $d \ln(\sigma)/dE$ for $\sigma_m(y)$ [Eq. (36), •] compared to $2C_\sigma f_\sigma(0)$ [Eq. (39)] and $\sigma_\lambda(y)$ [Eq. (41)]. In both cases, $K_s = 6$. Also shown are $d \ln(\kappa L)/dE$ (\diamond) and its limiting cases [Eq. (61)] (dashed lines). Axes of (a) and (b) plots are at different scales. Compare with Fig. 6.

IV. ANALYSIS

The effects of non-linearity of the barrier on the Gamow factor $\theta(E)$ and the energy slope factor $\beta_F(E)$ affect the evaluation of the current density J_S by affecting the integrand $dJ(E) = D(E)f(E)$ of Eq. (45) [and analogously for J_M and Eq. (46)]. The present section shall compare the integrands using Eq. (44) for $f(E)$ and Eq. (48) for $D(E)$, with the analysis focusing on the consequences of the approximations used for $\theta(E)$. The rapidity of the evaluation of $dJ(E)$ is substantially increased through the usage of the analytic approximations to $\sigma(y)$ that are available [Eq. (12) for $\sigma_0(y)$ and $\sigma_\gamma(\tilde{y})$ and Eq. (41) for $\sigma_\lambda(y)$], and which crucially enables the rapid determination of E_m on which the linear Gamow approximation of Eq. (49) on which $N(n, s)$ depends. Clearly, the behavior of $\sigma_m(y)$ in Fig. 6 suggests that simple and useful interpolative or approximate schemes of good accuracy can be tailor-made for conditions, but the usage of the analytic models, even if less accurate, enables reproducibility, and so shall be used instead. A comparison of three methods to find $dJ(E)$ will, therefore, give rise to the four forms of the Gamow factor and the tunneling probability:

1. an “exact” form using Eq. (6) for $\theta(E)$ and analytic forms of $\sigma[y(E)]$ as specified,
2. a “linear- θ ” form using Eq. (49) with E_m requiring determination and $\beta_F(E)$ from $\theta(E)$ using finite difference methods,
3. a “conventional” form using the Fowler–Nordheim [Eq. (A6)] form of $D(E)$ as commonly done for depletion and MIM-like barriers, and
4. a “conventional” form using the Richardson/Bethe ($\Theta[E - V(x_o)]$) form of $D(E)$ as commonly done for depletion and MIM-like barriers

for which Forms 3 and 4 are both cases of the “conventional” form but are treated separately. For convenience, the current integrand of $J_S(F, T)$ [Eq. (45)] is treated for simplicity; the treatment for J_M proceeds analogously. The final evaluation of $J_S(F, T)$ using Form 1 requires numerical integration, whereas Forms 2 and 3 allow for using Eqs. (51), (C4), or (C5) as circumstances allow or numerical integration if convenient.

A. Depletion barrier: Tunneling

Consider conditions where $dJ(E)$ is dominated by tunneling contributions for the depletion barrier of Eq. (13) with $V_o = \mu + \Phi$ over a range of energies E (thermal emission studies are deferred to Sec. IV B because here, near the apex, the depletion barrier resembles a Schottky–Nordheim barrier and, therefore, inferences based on general thermal-field analyses are sufficient). The evaluation of $V(x_o)$, $\kappa(E)$, and $L(E)$ all rely on numerically determining the roots $x_j(E)$ and the location of the maximum x_o . For $E = 0$, $x_2(0) = x_3(0) = x_h$. For $E_{N+1} = V(x_o)$, $\theta(E_{N+1}) = 0$ and $\beta_F(E_{N+1})$ is given by Eq. (56) with $y = 1$. As a computational matter, it is more convenient to specify the roots $x_1(0)$ and $x_2(0)$ for a given K_s (and hence $Q_s = Q/K_s$) rather than specify V_o and F and determine the roots thereafter, as the potential barrier factors are quickly and explicitly determined by equating Eq. (1) to

$$V_\gamma(x) = \frac{\gamma}{x} [x_1(0) - x][x_2(0) - x][x_3(0) - x], \quad (62)$$

a form implicit in Eqs. (17) and (18). It follows:²⁷

$$\begin{aligned} \gamma &= Q_s x_1 x_2 x_3, \\ F &= \gamma(x_1 + x_2 + x_3), \\ V_o &= \gamma(x_1 x_2 + x_1 x_3 + x_2 x_3), \\ x_o &= \left[\frac{Q_s}{F - 2\gamma x_o} \right]^{1/2}, \end{aligned} \quad (63)$$

where $x_j(0) \rightarrow x_j$ for convenience, $x_2 = x_3 = x_h$ is understood, and the equation for x_o may be solved by iteration starting from an initial value of $x_o \approx \sqrt{Q_s}/F$ with convergence achieved after five to eight iterations. Three examples are shown in Fig. 10.

To evaluate $\theta(E)$ on a set of $E_i = iV(x_o)/(N + 1)$ and $i \in (0, 1, 2, \dots, N)$, the roots $x_j(E_i)$ must first be identified. Although the E_i so defined is equi-spaced, that is not required. A rapid and systematic method to do so is by Newtonian iteration, for which the roots for $E_0 = 0$ have already been specified by $x_2(0) = x_h$ and $x_1(0)$. Letting $x_j(0) = x_j$ for $j \in (1, 2, 3)$, then

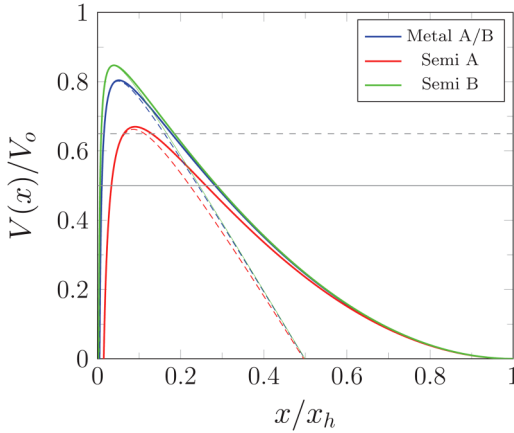


FIG. 10. Barriers $V_\gamma(x)$ constructed using the $(K_s, x_1(0), x_h)$ parameters of Table III with $x_2(0) = x_3(0) = x_h$. Thin red and blue dashed lines correspond to $\gamma = 0$ (linear barrier). The thin horizontal gray line corresponds to $\mu/V_o = 0.5$ (Metal A and Semi-A/B) and the thin horizontal gray dashed line to $\mu/V_o = 0.65$ (Metal B).

from Eq. (62),

$$V'(x) = \frac{\gamma}{x^2} [x_1 x_2 x_3 - (x_1 + x_2 + x_3 - 2x)x^2], \quad (64)$$

where $x_2(0) = x_3(0) = x_h$ in the present case. The solution of $V[x_j(E_i)] - E_i = 0$ defines $x_j(E_i)$ and is found by repeatedly performing

$$\bar{x} \leftarrow \bar{x} - \frac{V(\bar{x}) - E_i}{V'(\bar{x})} \quad (65)$$

until convergence, using $\bar{x} = x_j(E_{i-1})$ as the initial value. After convergence, then $\bar{x} \rightarrow x_j(E_i)$. For closely spaced E_i , convergence is very rapid, with convergence after three iterations being adequate. For finding the smaller root, the iteration for $x_1(E_1)$ can begin with $\bar{x} = x_1(0)$, but not so for $x_2(E_1)$ because $V'[x_2(0)] = 0$ by definition. Therefore, for the larger root starting value, the parabolic nature of $V(x)$ near $x = x_h$ allows the initial \bar{x} to be taken as $\bar{x} = x_h - \delta$ with δ small (e.g., $\delta = 0.02$) from which $x_2(E_1) = x_h - \delta \sqrt{E_1/V'(\bar{x})}$. Because $x_1(E_i)$ monotonically and smoothly increases with i and $x_2(E_i)$ monotonically decreases, in practice, E_i need not be finely spaced, and interpolation to intermediate values can be used to reduce computational overhead, but because the convergence is rapid already, this approach is not used in the present study. Parenthetically, it is observed that the process could just as well begin starting at $j = N$ with $x_1(E_{N+1}) = x_2(E_{N+1}) = x_o$ and find the $(j - 1)$ th roots from the j th roots, as would be advantageous if only a small energy range below the Fermi level is desired.

With the roots in hand, then a straightforward evaluation yields

$$\kappa(E_i) = \left[\frac{2m}{\hbar^2} (V(x_o) - E_i) \right]^{1/2}, \quad (66)$$

$$L(E_i) = x_2(E_i) - x_1(E_i),$$

$$\sigma[y(E_i)] \approx \sigma_0[\tilde{y}(E_i)],$$

where Eq. (12) is used for $\sigma_0(y)$, $\tilde{y}(E) = (y - y_{min})/(1 - y_{min})$ as per Eq. (26), and $y_{min} \equiv [V_o - V(x_o)]/V_o$ [a simplification of Eq. (19) when $V(x_h) = 0$]. From these components, then $\theta(E) = 2\sigma(y)\kappa(E)L(E)$ provides the Gamow factor (Form 1), and

$$\beta_F(E_i) \approx - \frac{\theta_{i+1} - \theta_{i-1}}{E_{i+1} - E_{i-1}} \quad (67)$$

[compare Eq. (60)] is the finite difference approximation to the derivative, giving the slope factor $\beta_F(E)$ [an upwind/downwind second order difference $\mp(3\theta_i - 4\theta_{i\pm 1} + \theta_{i\pm 2})/2$ is used for the end points $i = 1$ and $i = N + 1$]. Observe that this method incorporates the weak dependence of $\sigma(y)$ on E ; that is, the constant- σ approximation is not used. The performance of Forms 2 and 3 can now be compared to Form 1.

Using the parameters of Table III, the integrand $dJ(E)$ is shown using the exact $\theta(E)$ (Form 1, symbol \circ) compared to the linear- θ (Form 2, red line) and the FN (Form 3, blue line) in Fig. 11. The Metal-B case results in parameters typical of tungsten. The Semi-A/B cases are typical of semiconductor parameters. The area of the light gray shaded region is proportional to J_S (J_θ and J_{FN} would likewise correspond to the areas under their respective curves). The closer μ is to $V(x_o)$, the better J_{FN} approximates J_S , but several mitigating factors are apparent. Normally as the temperature increases, more of the integrand enters the energy range between μ and V_o (the TF regime), making agreement between J_{FN} and J_S seemingly improved when in fact the shapes of the integrands have significantly diverged. In the case of Semi-B, the TF

TABLE III. Metal-like and semiconductor-like parameters. Column labels correspond to labeling in Fig. 11.

Term	Metal A	Metal B	Semi-A	Semi-B
Independent terms				
T (K)	300	1600	300	230
K_s	1	1	6	12
x_1 (nm)	0.02	0.02	0.06	0.03
x_h (nm)	4	4	4	10
μ/V_o	0.50	0.65	0.50	0.50
Dependent terms				
V_o (eV)	18.18	18.18	1.03	1.01
x_o (nm)	0.205	0.205	0.362	0.395
$V(x_o)$ (eV)	14.62	14.62	0.690	0.853
F (eV/nm)	9.022	9.022	0.504	0.200
γ (eV/nm ²)	1.125	1.125	0.0625	0.010
y_{min}	0.196	0.196	0.330	0.153
J_θ/J_S	1.028	1.042	1.099	1.288
J_{FN}/J_S	16.94	2.045	1.938	1.209

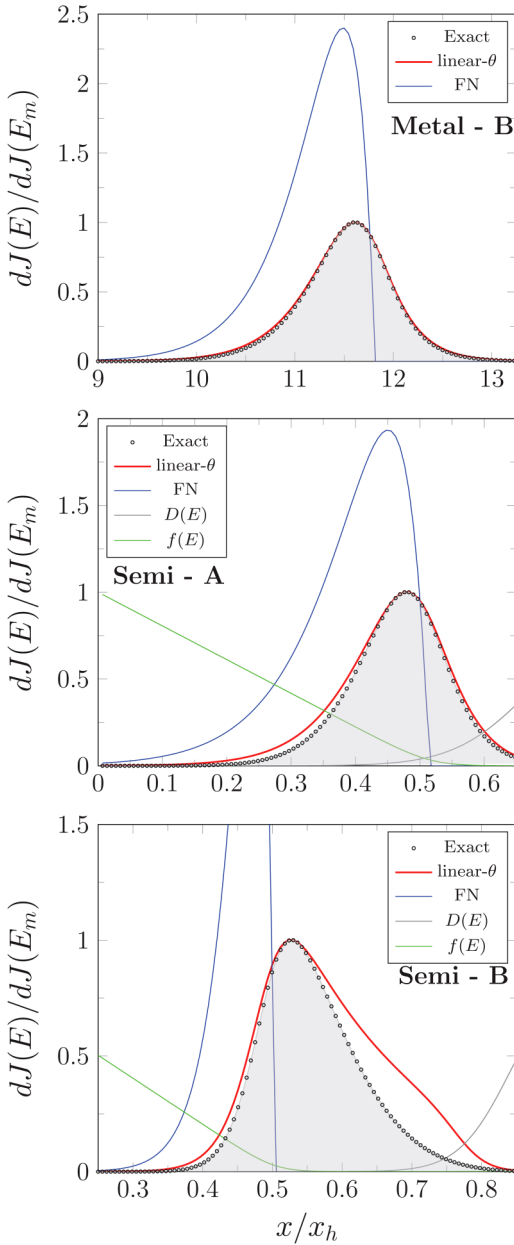


FIG. 11. Comparison of the exact, linear- θ , and FN forms of $\theta(E)$ as used in $dJ(E)$ for the parameters of Table III, normalized to $dJ_S(E_m)$. Observe that in Semi-B, conditions are such that the TF regime has been entered. The gray area is proportional to J_S ; J_θ and J_{FN} correspond to the area under the red and blue curves, respectively.

regime has been entered *even though the temperature appears small*, and therefore, J_θ is larger than it should be (larger, in fact, than J_{FN} , even though the FN approximation is clearly worse). Methods to account for the over-estimation in the TF regime for

the linear barrier model⁸⁹ can be used to correct the overestimation. The ratios between J_θ and J_{FN} with J_S are shown in Table III. In all cases (even the seemingly worse Semi-B), the estimate of the current density using the linear- θ (Form 2) approximation is superior to the Fowler–Nordheim (Form 3) approximation.

B. MIM barrier

The analysis is now repeated for the case of the more complex MIM-like barrier in which $V_m(x)$ of Eq. (2) is given by Eq. (31) with $s = x/W$. Two kinds of comparisons are made: first, in a tunneling regime and second, in a thermal regime. For purposes of comparison, the Fermi level is set to a fraction of the barrier height parameter via a ratio factor r , as in $\mu = rV_o$, with $r = 1/2$ being the default choice so that the work function is $\Phi = (1 - r)V_o$.

The investigation of thermal emission requires addressing how $D(E)$ behaves as E exceeds V_o . Theoretical models⁵ indicate that $\theta(E)$ and $\beta_F(E)$ are continuous across the boundary $E = V(x_o)$, and therefore, a reasonable approximation is to set

$$\theta[V(x_o) - \Delta] = -\theta[V(x_o) + \Delta], \quad (68)$$

where $\Delta = |V(x_o) - E|$, for which the Kemble approximation suggests $D[V(x_o)] = 1/2$, a relation exact for parabolic potentials but requiring modification for triangular and rectangular ones: the apex of depletion and MIM barriers including image charge modifications are approximately parabolic and, therefore, amenable to the approximation. As before, the analysis is undertaken by examining the behavior of $dJ(E)$, but now the energy range is extended to above the barrier maximum $V(x_o)$ so as to examine the thermal regime. In contrast to the depletion barriers, however, at low fields where $FW < \Phi$, the Fowler–Nordheim parameterization will significantly overestimate $\theta(E)$ because it assumes values of $L(E)$ that are larger than the width W of the MIM barrier; at high fields where $FW > \Phi$, the correspondence will be analogous to the findings of Sec. IV A and, therefore, have already been treated. Consequently, for the MIM barrier treatment, the analysis will shift to examine the accuracy of the purely analytic approximation $\sigma_m(y) \approx \sigma_\lambda(y)$ of Eq. (41), for which no factors must be pre-calculated. The asymptotic behavior of Eqs. (39) and (40), however, suggests a final “semi-analytic” form that modifies $\sigma_\lambda(y)$ of Eq. (41) through the evaluation of $\sigma_m(y)$ at only two values of y , but which enables a relatively good approximation with otherwise minimal effort, given by

$$\begin{aligned} \sigma_{<}(y) &= \frac{\pi}{4} - \left(\frac{\pi}{4} - \sigma_N\right) \left[\frac{1-y}{1-y_N}\right], \\ \sigma_{>}(y) &= 1 + [\sigma_1 - 1] \left(\frac{y}{y_1}\right), \\ \sigma_\alpha(y) &\equiv \max[\sigma_{<}(y), \sigma_{>}(y)], \end{aligned} \quad (69)$$

where σ_1 and σ_N could be approximated using Eqs. (39) and (40) but (as shall be done here) are better given by $\sigma_m(y_1)$ and $\sigma_m(y_N)$, respectively, where $y_j = j/(N + 1)$ and N is the number of points used for the coarse-gridding of E_j from which the spline approximation to $\theta(E)$ is constructed: such an approach requires only two

numerical integrations rather than N , and the resulting form enables the rapid evaluation of E_m needed for constructing $dJ(E)$. A comparison of $\theta(E)$ via Eq. (6) evaluated using numerically determined values of $\kappa(E)$ and $L(E)$ is shown in Fig. 12 with $\sigma(y)$ given by the exact $\sigma_m(y)$ [Eq. (36)], the purely analytic $\sigma_\lambda(y)$ [Eq. (41)], and the semi-analytic $\sigma_a(x)$ [Eq. (69)].

Rapid and repeated evaluations of $dJ(E)$ to find E_m from which $\theta(E_m)$ and $\beta_F(E_m)$ are obtained and from which $J_{GTF}(E, T)$ is determined are now possible because the requirements for numerical integration in the evaluation of $\sigma_m(y)$ have been eliminated. Although the search algorithms [to find the roots $s_j = x_j/W$ on which $\kappa(E)$ and $L(E)$ depend] are rapid, the execution speed can be enhanced further by evaluating $\kappa(E)L(E)$ on a coarse grid of E_j values: the smoothness of $\theta(E_j)$ then allows for either a rapid spline-fitting algorithm to construct $\theta(E) = 2\sigma\kappa L$ for arbitrary values of energy (the method used below) or an approximation of $\theta(E) = \sum_j C_j E^j$ by a cubic equation for which the coefficients C_j are determined by $\theta(E)$ and $\beta_F(E)$ at $E = \mu$ and $E = V(x_0)$ as for the simple GTF model.^{27,98} As a result, the determination of E_m , $\theta(E_m)$, and $\beta_F(E_m)$ can be made in a computationally expedient manner. Three sample cases are considered to demonstrate the performance: (i) a field-dominated (low temperature) condition, (ii) a temperature-dominated (high temperature) condition, and (iii) a mixed (intermediate temperature) condition.

In particular, case (iii) demonstrates how reliance on either a Fowler–Nordheim characterization when tunneling is presumed dominant or a Richardson/Bethe characterization when thermal transport is presumed dominant can substantially overlook effects that contribute, apart from the other issues identified with their usage described previously.

A comparison of the numerically intensive evaluation of $dJ(E)/dE = D(E)f(E)$ (the integrand of Eq. (45); for convenience, J_S rather than J_M is treated) using the exact evaluation of $\sigma_m(y)$ is

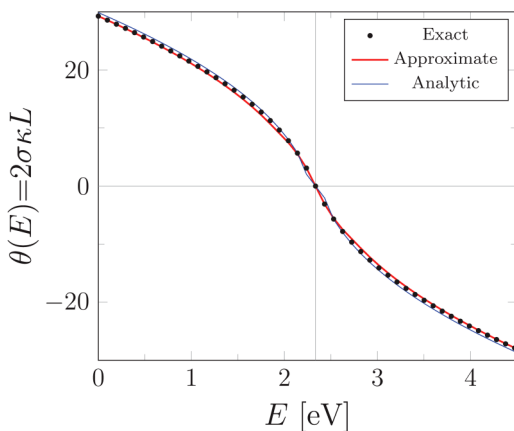


FIG. 12. Comparison of the exact [Eq. (36)], analytic [Eq. (41)], and approximate [Eq. (69)] forms of $\theta(E)$ over the range for which $dJ(E)$ as a function of temperature will be evaluated in Fig. 13 for the parameters $V_0 = 2.5$ eV, $F = 0.1$ eV/nm, $W = 2$ nm, and $K_S = 6$. Gray horizontal line is at $\theta = 0$, and the gray vertical line is at $E = V(x_0)$.

compared to that obtained using the approximate $\sigma_a(y)$ and analytic $\sigma_\lambda(y)$ in Fig. 13 for temperatures for which field (300 K), thermal (1000 K), and mixed (720 K) conditions dominate. The small differences between $\theta(E)$ and its approximations are more clearly visible in the $dJ(E)$ behaviors. The gray area is, as with

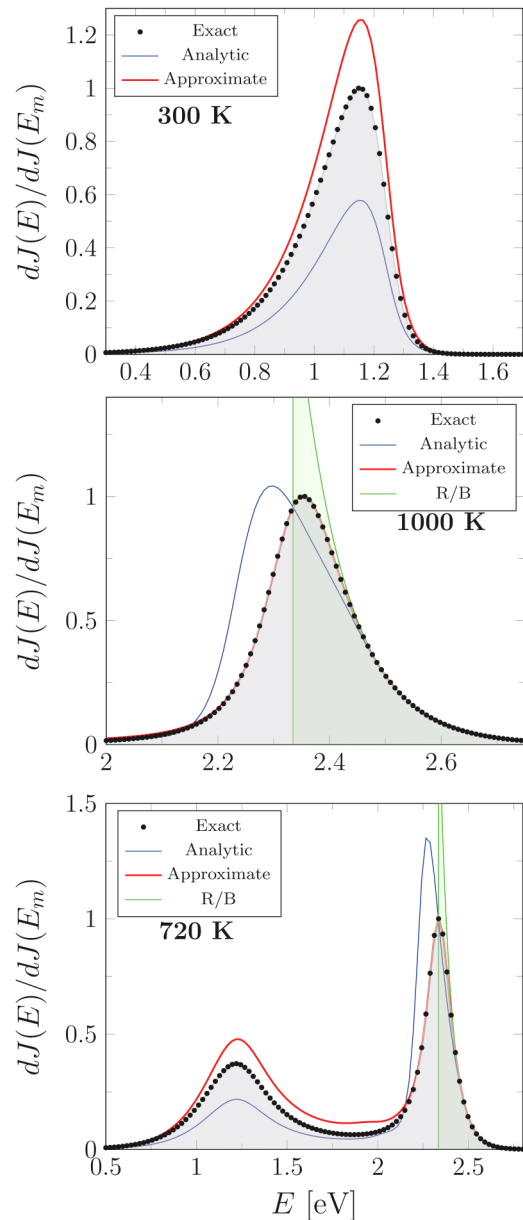


FIG. 13. Evaluation of $dJ(E)$ for the $\theta(E)$ factors and parameters of Fig. 12 using the exact [Eq. (36)], analytic [Eq. (41)], and approximate [Eq. (69)] forms of $\theta(E)$. The green region (when visible) shows the Richardson/Bethe (R/B) model, for which $D(E) = \Theta[E - V(x_0)]$. The gray region is proportional to J_S . The Fermi level $\mu = V_0/2 = 1.25$ eV.

Fig. 11, proportional to the current density: it is apparent that even if the integrated areas are comparable, the underlying behavior of the integrands can be substantially different: these differences would, for example, affect the distribution of energies required in beam optics simulations discussed in Sec. I. In the case of the mixed conditions, moreover, a purely thermal (Richardson/Bethe) or field (Fowler–Nordheim) model would completely miss contributions: the behavior of $dJ(E)$ for the MIM barrier in these cases exhibits behavior more extreme than that found in the Schottky–Nordheim potentials often assumed in the canonical equations, for which the energy distributions, both theoretically^{87–89,99} and experimentally,^{100,101} are characterized by a single peak that broadens in the thermal-field regime (the beginnings of which is seen in the “Semi-B” figure of Fig. 11). The double-peak behavior in the thermal-field (TF) regime indicates that although the linear Gamow approximation of Eq. (49) is useful in either the thermal or field regimes for the MIM barrier, in the TF regime, the full non-linear behavior of $\theta(E)$, evident in Fig. 12, becomes consequential near the barrier maximum: the development of an analytic equation for J_S (or J_M) in the TF regime will require methods for accounting for the non-linear features of $\theta(E)$ beyond those of Appendix C and the usage of Lorentzian correction factors for the Schottky–Nordheim barrier.⁸⁹

The suggestion in Fig. 13 that the analytic model performs reasonably if not adequately in the TF regime needs qualification. In the TF regime of different conditions, such as a higher field, the departures can become more pronounced, an example of which is shown in Fig. 14, which highlights two kinds of defects in the analytic model of Eq. (41) that require attention in the TF regime, but for which the approximate model [Eq. (69)] remains good. First, the discontinuity in the slope of $\sigma_\lambda(y)$ at $\lambda = 1$, readily apparent in Figs. 6 and 9, results in the overestimation of $\sigma(y)$ even if κL is evaluated well: this defect is responsible for the plateau-like

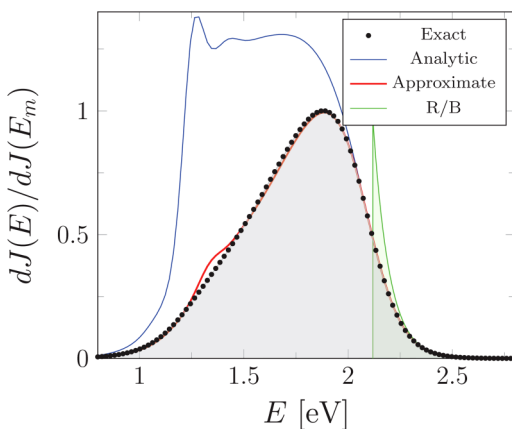


FIG. 14. Same as Fig. 13 but for $F = 0.6$ eV/nm and $T = 900$ K, showing the conditions under which the analytic form of $\sigma(y)$ degrades, but for which the approximate form is adequate. The ripples in the analytic form are a consequence of the low number of points (24) used to construct the spline interpolant and not a defect of the analytical model itself.

behavior for $\mu \lesssim E \lesssim V(x_0)$. Second, the change in the slope results in ripples in the spline approximation visible near $E = \mu$: the ripples are increasingly suppressed as the number of spline points is increased, and therefore, these ripples are a purely numerical artifact of the spline approach, not a defect of the analytic model itself. It may be concluded that the analytic equation (41) is sufficient for preliminary investigations of the behavior of $dJ(E)$, but that accuracy requires usage of the slightly more demanding approximate equation (69), with the caveat that the TF regime requires particular attention. Under many conditions, however, the narrow TF regime is expected to be but a small part of the performance conditions under which devices involving MIM barriers may be required to operate.

Compared to the Schottky–Nordheim and depletion barriers, the behavior of the MIM barriers (and barriers like them) contains more abrupt transitions caused by the passage of FL from smaller than $V_0 - E$ to larger (*i.e.*, from $\lambda < 1$ to $\lambda > 1$), and this results in greater complexity of the shape factor $\sigma(y)$: the TF regime is approached when $L(E)$ begins to vary rapidly with E instead of being close to W . As a result, the linear Gamow approximation of Eq. (49) and its usage in evaluating $J(F, T)$ in the GTF formalism of Sec. III and Appendix C requires greater care. Such considerations are of even greater consequence if the incident distribution, or supply function, of electrons is a consequence of thin layer processes in MOS and semiconductor field emitters¹⁰² and nanogaps, or excitation and generation as occurs for photoemission⁴ and detectors.^{29,103} In such cases, usage may be made of the approximation approach behind Eq. (69) and its usage with $\kappa(E)L(E)$ found numerically, which, though requiring more computations than conventional methods based on FN and R/B behavior, nevertheless performs with sufficient rapidity to enable simulation of current flow under more complicated conditions. Efforts to do so shall be reported separately.

V. CONCLUSION

A recent formalism based on the shape factor^{5,104} and thermal-field methods^{86,87,89} has been used to accurately model emission through and over barriers associated with depletion layers, nanotip barriers, and MIM/MIS/MOS structures. The transmission probability is accurately modeled as the electron energy approaches and surpasses the barrier height using analytically motivated approaches useful to simulation codes. The methods have applications to more general barriers and are designed to satisfy the need for rapid but accurate models when a range of energies and/or a large distribution of contributing particles are present (e.g., thermal-field conditions, photoexcited distributions, etc.), as for device modeling needs and electron beam codes. Importantly, the analytical models of the transmission probability are designed to supersede the canonical emission equations used by depletion and MIM barrier studies. By separating the Gamow tunneling factor $\theta(E)$ into the product of a dimensionless shape factor $\sigma(y)$ and an easily evaluated tunneling integrand height and the width factor $2\kappa(E)L(E)$, the dominant contribution of the later to the Gamow factor $\theta(E)$ and the energy slope factor $\beta_F(E)$, which are the primary determinants of transmission probability, can be identified and isolated, thereby enabling methods that ease

numerical demands that complicate theoretical methods of acquiring $\theta(E)$. In this work, we have provided rapid means to analyze two classes of barriers defined by zeros of a polynomial function, have shown how to calculate the roots of those polynomials quickly, and have described the resultant linearized Gamow factors. From those factors, the impact on the current density through, over, or past the non-linear barriers was examined in a manner that is computationally advantageous to device simulation and emitter characterization for technologically interesting barriers characteristic of a range of emergent technologies.

ACKNOWLEDGMENTS

This work was supported in part by the Los Alamos National Laboratory (LANL) Directed Research and Development (LDRD) Funds and partly conducted at the Center for Nonlinear Studies (CNLS) and the Center for Integrated Nanotechnologies (CINT), U.S. Department of Energy (DOE). This research used resources provided by the LANL Institutional Computing (IC) Program. LANL is operated by Triad National Security, LLC, for the National Nuclear Security Administration of the U.S. Department of Energy (Contract No. 89233218NCA000001). This manuscript has been authored by UT-Battelle, LLC, under Contract No. DE-AC05-00OR22725 with the U.S. Department of Energy. Additionally, this work was supported by the Air Force Office of Scientific Research (AFOSR) through the lab task (No. 18RDCOR016). We thank M. McDonald (NRL), J. Harris, J. Riga, and J. Connelly (AFRL), and J. Smedley, K. Nichols, and H. Andrews (LANL) for profitable discussions.

APPENDIX A: FOWLER NORDHEIM BARRIER

The triangular barrier model of Fowler and Nordheim⁴⁷ is the simplest leading order approximation to depletion barriers^{64,67,105–107} and metal–insulator–metal (MIM) or metal–insulator–semiconductor (MIS) and metal–oxide–semiconductor (MOS) barriers^{94,108–110} subject to a high bias potential. Approximations used in the development of the Fowler–Nordheim Equation (FNE),⁴⁷ therefore, retain a presence in the shape factor analysis of Sec. II A. Those approximations are briefly recounted.

The triangular barrier is characterized by a potential of the form $V(x) = V_o - Fx$ with $V_o = \mu + \Phi$ for metals; and therefore, the associated Gamow factor $\theta(E)$ is the $y = 0$ limit of Eq. (6) for which $\sigma(y) \rightarrow \sigma(0) = \sigma_\Delta = 2/3$ as in Eqs. (12) and (28). From the relations $\hbar^2 \kappa(E)^2 / 2m = V_o - E$ and $L(E) = (V_o - E) / F$, it follows that

$$\theta(E) = \frac{4}{3} \kappa(E) L(E) = \frac{4}{3\hbar} \sqrt{2m(\mu + \Phi - E)^3}. \quad (A1)$$

The Fowler–Nordheim equation for the current density $J_{FN}(F)$ chooses $E_m = \mu$ in Eq. (49), leading to

$$\theta(\mu) = \frac{4}{3\hbar F} \sqrt{2m\Phi^3}. \quad (A2)$$

Likewise, the energy slope factor $\beta_F(E) = -\partial_E \theta(E)$ of Eq. (53) gives

$$\beta_F(E) = \frac{2}{\hbar F} \sqrt{2m(\mu + \Phi - E)} \quad (A3)$$

so that $\beta_F(\mu) = 2\sqrt{2m\Phi} / \hbar F$. Finally, the low-temperature limit of Eq. (51) sets $n \gg 1$, and therefore, Eq. (51) returns,^{51,61}

$$\lim_{T \rightarrow 0} J_{GTF}(F, T) = A_{RLD} T^2 \left[\frac{\beta_T}{\beta_F(E_m)} \right]^2 e^{-\theta(E_m)}. \quad (A4)$$

Using $A_{RLD} \equiv m q k_B^2 / 2\pi^2 \hbar^3 = 120.173 \text{ Amp/K}^2 \text{ cm}^2$ and $\beta_T = 1/k_B T$ and $E_m \approx \mu$, this becomes

$$J_{FN}(F) = \frac{qF^2}{16\pi^2 \hbar \Phi} \exp\left(-\frac{4\sqrt{2m\Phi^3}}{3\hbar F}\right) \quad (A5)$$

and is equivalent to the *original* Fowler Nordheim equation⁴⁷ when $F \rightarrow q\mathcal{E}$, apart from a coefficient $P(\mu, \Phi) = 4\sqrt{\mu\Phi} / (\mu + \Phi)$ of order unity ($P = 2$ if $\mu = \Phi$).^{47,61,90}

For non-zero y , that is, when the Schottky–Nordheim barrier is used, then $J_{GTF}(F, 0)$ is equivalent to the Murphy and Good $J_{MG}(F)$ version, as can be shown.^{51,61} Briefly, in a conventional Fowler–Nordheim analysis, $\theta(E)$ is approximated by

$$\begin{aligned} \theta_{FN}(E) &= \theta(\mu) - \beta_F(\mu)(E - \mu), \\ \theta(\mu) &= \frac{4}{3\hbar F} \sqrt{2m\Phi^3} v(y), \\ \beta_F(\mu) &= \frac{2}{\hbar F} \sqrt{2m\Phi} t(y) \end{aligned} \quad (A6)$$

using the Schottky–Nordheim parameters $v(y)$ and $t(y)$ ^{51,61} [in the reformulated *GTF* approach, these factors are displaced in favor of $\sigma[y(E)]$, but for $E = \mu$, the results are equivalent⁸⁷—see Eqs. (A4) and (A5) of Ref. 86 for the connection}. Using the Forbes–Deane approximations¹¹¹ to $v(y)$ and $t(y)$, J_{MG} can be expressed as [compare Eq. (B2) of Ref. 89 and discussions therein]

$$J_{MG} = \frac{qF^2}{16\pi^2 \hbar \Phi t_o^2} \left[\frac{e^3}{y(\mu)} \right]^{2\nu} \exp\left(-\frac{4\sqrt{2m\Phi^3}}{3\hbar F}\right), \quad (A7)$$

with $\nu = (8Q_s / 9\hbar) \sqrt{2m/\Phi}$, $t(y) \approx t_o = 1 + (1/6e) = 1.0613$, and $y(\mu)$ from Eq. (8), with the rendering purposely intended so as to preserve the visual similarity to Eq. (A5), although it obscures that the power p of F^p in the coefficient is $p = (2 - \nu)$ rather than 2 because of the field dependence of $y(\mu)$. For example, for $K_s = 1$ and $\Phi = 2 \text{ eV}$, then $\nu = 0.1932$.

APPENDIX B: QUADRATIC BARRIERS

1. Doping and depletion

A simple doping profile $V_d(x)$ is obtained for a dielectric of thickness L and dielectric constant $K_s \epsilon_0$ subject to a vacuum field

by solving Poisson's equation,

$$\partial_x^2 V_d(x) = \frac{q^2 N_d}{K_s \epsilon_0} = \frac{8\pi Q}{K_s} N_d \equiv 2\gamma, \tag{B1}$$

where the units of $V_d(x)$ are in eV as a result of multiplying both sides by the electron charge ($-q$) so that the customary negative sign is absent, and similarly, $F = -q\mathcal{E}$ is in units of eV/nm. Subject to the conditions

- $V_d(x)$ is equal to V_o at the origin and vanishes at the depletion width w ,
- the gradient of $V_d(x)$ is continuous at $x = w$ and equals $(F_{vac}/K_s) \equiv -F$ at $x = L$,
- dopants are only ionized for $x \leq w$ such that N_d is a constant, and therefore, $V_d(0 \leq x \leq w) = A + Bx + Cx^2$ and $V_d(w < x \leq L) = D + Gx$,

then Eq. (B1) can be cast as a matrix equation given by

$$\begin{bmatrix} 0 & 0 & 1 & 0 & 0 \\ 1 & w & -1 & -w & -w^2 \\ 0 & 1 & 0 & -1 & -2w \\ 0 & 1 & 0 & 0 & 0 \\ 0 & 0 & 0 & 0 & 2 \end{bmatrix} \begin{bmatrix} A \\ B \\ C \\ D \\ G \end{bmatrix} = \begin{bmatrix} V_o \\ 0 \\ 0 \\ -F \\ 2\gamma \end{bmatrix}. \tag{B2}$$

Inverting and collecting, $V_d(x)$ is given by

$$V_d(x) = \begin{cases} V_o - (F + 2\gamma w) + \gamma x^2 & (x \leq w), \\ V_o - \gamma w^2 - Fx & (x > w). \end{cases} \tag{B3}$$

The depletion width w where $V_d(w) = 0$ is given by

$$w(F) = \frac{2V_o}{F + \sqrt{4\gamma V_o}}. \tag{B4}$$

For $F = 0$, the usual depletion width $w(0) = \sqrt{V_o/\gamma} = \sqrt{2K_s \epsilon_0 V_o / q^2 N_d} = \sqrt{K_s V_o / 8\pi N_d Q}$ is obtained. If the right contact is held at V_a instead of subject to a vacuum field term F_{vac} , then V_a is the solution to $V_a = V_o - \gamma w^2 - FL$. An example for generic parameters is shown in Fig. 15.

2. Prolate spheroidal emitter

The potential barrier associated with field emission from a prolate spheroidal emitter^{75,77} is well modeled by a quadratic potential.²⁷ The prolate spheroidal diode equipotentials are governed by hyperbolic surfaces of v in prolate spheroidal coordinates (v, η) , related to cylindrical coordinates (ρ, z) by

$$\begin{aligned} \rho &= L \sinh(\eta) \sin(v), \\ z &= L \cosh(\eta) \cos(v), \end{aligned} \tag{B5}$$

in which Laplace's equation becomes

$$(\sin v \partial_v^2 + \cos v \partial_v) V_h(v) = 0, \tag{B6}$$

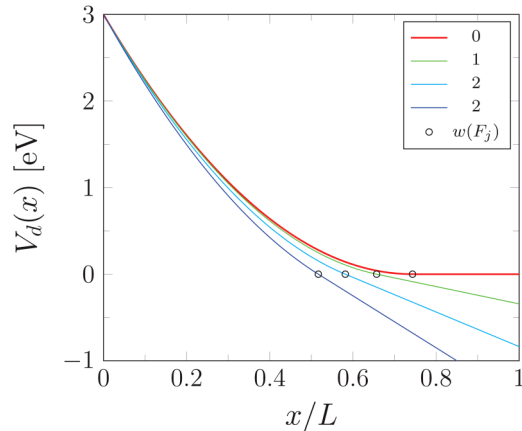


FIG. 15. The behavior of $V_d(x)$ given by Eq. (B3) for generic semiconductor parameters of $K_s = 6$, $V_o = 3$ eV, $N_d = 10^{16}$ cm⁻³, $L = 0.6$ μm, and fields of $F_j = 0.01j/K_s$ (eV/nm). The lines are labeled by the values of $F_j L$. Black o's are locations of $V_d[w(F_j)]$ via Eq. (B4), for which $w(0) = \sqrt{V_o/\gamma}$.

where the anode is specified by $v = \pi/2$ and the emitter surface by v_o . Solutions are

$$\begin{aligned} V_h(v) &= V_o \left(1 - \frac{Q_0(\cos v)}{Q_0(\cos v_o)} \right), \\ Q_0(s) &\equiv \frac{1}{2} \ln \left(\frac{1+s}{1-s} \right), \end{aligned} \tag{B7}$$

where $Q_0(s)$ is a Legendre polynomial of the second kind. Electrons that follow the field lines (along constant η) tunnel through a potential given by

$$V[x(\eta, v)] \equiv \mu + \Phi + V_h(v) - \frac{Q}{x(\eta, v)} \tag{B8}$$

$$\approx \mu + \Phi - F_\eta x + \gamma_\eta x^2 - \frac{Q}{x}, \tag{B9}$$

where a different F_η and γ_η is required for each emission site along the surface, and

$$x(\eta, v) = L \int_{v_o}^v \sqrt{\sinh^2 \eta + \sin^2 u} du \tag{B10}$$

such that $x(\eta, v_o)$ is on the emitter and $x(\eta, \pi/2)$ terminates on the anode plane, with the notational choice of $x(\eta, v)$ to reinforce that it is analogous to the distance from the surface in a 1D tunneling problem. For simplicity here, consider the on-axis trajectory, and let $F_\eta \rightarrow F$ and $\gamma_\eta \rightarrow \gamma$. Consequently, for $(\eta = 0)$, $x(v, 0) = L(\cos v_o - \cos v)$ and

$$F = \frac{V_o}{L \sin^2 v_o Q_0(\cos v_o)}, \tag{B11}$$

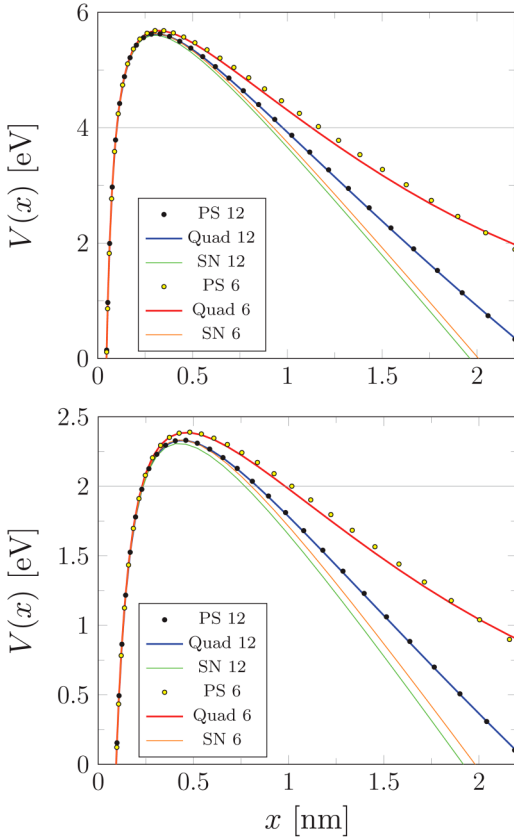


FIG. 16. (top) $V(x)$ as given by Eq. (B8) (\circ, \bullet), compared to Eq. (B9) (red and blue lines) apex radii of 4 nm and 12 nm, respectively, and the Schottky–Nordheim barrier (orange and green lines) for $\mu = 4$ eV, $\Phi = 4$ eV, $F = 4$ eV/nm and $\gamma = 0.264$ and 0.559 eV/nm², respectively. (bottom) The same as top, but for $\mu = 2$ eV, $\Phi = 2$ eV, $F = 2$ eV/nm, and $\gamma = 0.130$ and 0.270 eV/nm², respectively. Gray lines are μ .

with γ as determined by the methods of Refs. 27 and 61. Comparisons of Eqs. (B8) and (B9) and the Schottky–Nordheim ($\gamma = 0$) barrier (labeled “PL,” “Quad,” and “SN,” respectively) are shown in Fig. 16 for two values of the apex radius $a = 12$ nm and 4 nm each. In both cases, the quadratic model is visibly superior to the linear model, particularly near the Fermi level, although the analytic nature of Eq. (B9) would allow using shape factor methods directly on $V[x(\eta, \nu)]$.

3. Metal-insulator-metal

The designation of the “MIM barrier” is taken to refer to the metal-insulator-metal, metal-oxide-semiconductor, and other related barriers in which a thin layer is sandwiched between contacts, all of which may have different properties affecting the barrier height and supply functions. For the MIM barrier, the multiple image charge contribution $V_i(x)$ replaces the standard image

charge term Q_s/x . Recast Eq. (31) as

$$V_M(s) = \frac{2Q_s}{W} \frac{\nu(s)}{s(1-s)}, \quad (\text{B12})$$

which reproduces the approximation of Simmons⁸⁴ if $\nu(s)$ is replaced by a constant. Recall that the notation $x = sW$ is used and ($0 \leq s \leq 1$). The new function $\nu(s)$ is defined by

$$\nu(s) \equiv \frac{(1-s^2)(2bs^5 + 2as^3 + 1) + 2s^3}{2(s+1)} \quad (\text{B13})$$

and exhibits a concave up behavior for which $\nu(0) = \nu(1) = 1/2$ with a minimum of 0.346 539 at $s = 0.500$ 297. The zeros of $V_M(s)$ are the same as those of $V_M(s)s(1-s)$ and are always found using a combination of a bisection search to arrive in the vicinity of the root, followed by the Newtonian iteration for accuracy. The three quantities of the greatest importance are the roots s_1 and s_2 and the location of the maximum s_o .

a. Smallest root

Although the number of bisections and iterations required is typically small, for convenience, alternate iterative methods that are generally acceptable are possible. The first zero x_1 of $V_M(x_j) = 0$ may be obtained through iteration and is $x_1 = Ws_N$, where

$$s_{j+1} = \frac{2Q_s \nu(s_j)}{W(1-s_j)(V_o - WFs_j)}, \quad (\text{B14})$$

with $s_0 = Q_s/LV_o$. The convergence is rapid so that $N \geq 5$ provides a six digit accuracy.

b. Maximum location

The maximum x_o of $V_M(x)$ is the same as the zero of $P(s) = (W/Q_s)[s(1-s)]^2 \partial_s V_M(Ws)$, which varies between ± 1 with a single root. A robust method to find x_o is by using a bisection on $P(s)$ followed by a Newtonian iteration in which $s_{j+1} = s_j - P(s_j)/\partial_s P(s_j)$. If the barrier shape is not too trapezoidal, an iterative approach is possible by introducing

$$P(s) = h(s) - \frac{FW^2}{Q_s} s^2(1-s^2), \quad (\text{B15})$$

$$h(s) = -(1-s)^2[1 - 4as^3 - 8bs^5] - \frac{4s^3}{(1+s)^2}$$

and then iterating

$$s_{j+1} = \left(\frac{Q_s}{FW^2} \right)^{1/2} \frac{\sqrt{h(s_j)}}{1-s_j} \quad (\text{B16})$$

starting from the initial value of $s_0 = \sqrt{Q_s/FW^2}$ until convergence is achieved.

c. Largest root

Last, the larger zero x_2 of $V_M(x_j) = 0$ is found herein using a bisection on $V_M(x)$ for $x_0 < x < 1$ followed by a Newtonian iteration for a rugged procedure, but given the relative linear nature of

$$Z(s) = s(1 - s)V_M(s), \tag{B17}$$

a good initial choice rapidly returns the root via

$$s_{j+1} = s_j - \frac{Z(s_j)}{Z'(s_j)}, \tag{B18}$$

where

$$Z'(s) = (1 - 2s)(V_o - FWs) - \frac{2Q_s}{W}v'(s) - WFs(1 - s) \tag{B19}$$

and where $v'(s) = dv/ds$ is the derivative of Eq. (B13). Letting $s_0 = 0.5$ if $V_M(x_0) < FW$ and $s_0 = 0.99$ if $V_M(x_0) > FW$ generally (but not always) provides a good initial guess depending on parameters. Subsections 3 a–3 c of Appendix B assumed $E = 0$, but the analysis proceeds identically when $V_o \rightarrow V_o - E$.

APPENDIX C: GENERAL THERMAL-FIELD FUNCTION

Under conditions where both n and s are large, a common situation for thermal and field emission from metals, then an approximation to $N(n, s)$ of Eq. (52) takes the form⁸⁷

$$N(n, s) \approx e^{-s}n^2\Sigma\left(\frac{1}{n}\right) + e^{-ns}\Sigma(n), \tag{C1}$$

where the first term is identified with field-dominated emission and the second with thermal-dominated emission.^{51,87} For $x < 1$,

$$\Sigma(x) = \frac{1 + x^2}{1 - x^2} + 2 \sum_{j=1}^{\infty} [(1 - 2^{1-2j})\zeta(2j) - 1]x^{2j}. \tag{C2}$$

In practice, the first two terms of the sum in $\Sigma(x)$ of Eq. (C1) are sufficient (and even neglected), particularly when x is small, because $\zeta(2j)$ approaches unity rapidly, as can be seen by

$$\zeta(p) = \frac{2^p - 1}{2^p - 2} + \frac{1}{(1 - 2^{1-p})\Gamma(p)} \int_0^{\infty} \frac{x^{p-1} dp}{e^{2x}(1 + e^x)}, \tag{C3}$$

where $\Gamma(p)$ is the Gamma function. The first term dominates for large p and is close to unity.

It is seen that either $\Sigma(1/n)$ or $\Sigma(n)$ has an argument that exceeds unity, and therefore, in such cases, Eq. (C2) has divergent behavior as its argument becomes large, but the divergence is only as a power. The approximation of Eq. (C1), therefore, relies on the exponential smallness of e^{-s} or e^{-ns} , respectively, to suppress the diverging power behavior and retain a reasonable accuracy. For extremely high fields, e.g., when $y(E) \rightarrow 1$ in Eq. (16), the exponential arguments may not be sufficiently small, and the suppression

of $\Sigma(n)$ is not reliable. In such cases, the usage of Eq. (C2) causes $N(n, s)$ to begin decreasing and become negative as $y \rightarrow 1$. An expedient recourse is to approximate $N(n, s)$ by the larger of Eq. (C1) and n^2e^{-s} , as discussed in Ref. 89.

The connection to the canonical equations as limiting cases is trivially demonstrated when the linear Gamow approximation of Eq. (49) is used:

- **Field emission** Letting $E_m \approx \mu$, in the zero-temperature limit, the supply function $f(E) \propto (\mu - E)$ and $D(E) \approx e^{-X}$, where $X = \theta(\mu) + \beta_F(\mu)[\mu - E]$, and as a result,

$$J \propto e^{-\theta(\mu)} \int_0^{\mu} e^{-\beta_F(\mu)(\mu-E)}(\mu - E)dE = \frac{e^{-\theta(\mu)}}{\beta_F(\mu)^2}, \tag{C4}$$

where the integral $\int_0^{\alpha} e^{-x} dx \approx 1$ for a large α ; therefore, $J \propto T^2 n^2 e^{-s}$ with $s = \theta(\mu)$ and $\Sigma(1/n) \rightarrow 1$.

- **Thermal emission** Letting $E_m \approx \mu + \phi$, in the low field limit, the transmission probability $D(E) \approx \Theta(E - \mu - \phi)$ and $f(E) \propto e^{\beta_T(\mu-E)}/\beta_T$, and as a result,

$$J \propto \frac{1}{\beta_T} \int_{\mu+\phi}^{\infty} e^{\beta_T(\mu-E)} dE = \frac{e^{-\beta_T\phi}}{\beta_T^2}; \tag{C5}$$

therefore, $J \propto T^2 e^{-ns}$ with $s = \beta_T\phi$ and $\Sigma(n) \rightarrow 1$.

DATA AVAILABILITY

The data that support the findings of this study are available within the article.

REFERENCES

- ¹J. Schwede, T. Sarmiento, V. Narasimhan, S. Rosenthal, D. Riley, F. Schmitt, I. Bargatin, K. Sahasrabudde, R. Howe, J. Harris, N. Melosh, and Z.-X. Shen, *Nat. Commun.* **4**, 1576 (2013).
- ²J. W. Schwede, I. Bargatin, D. C. Riley, B. E. Hardin, S. J. Rosenthal, Y. Sun, F. Schmitt, P. Pianetta, R. T. Howe, Z.-X. Shen, and N. A. Melosh, *Nat. Mater.* **9**, 762 (2010).
- ³H. Yamaguchi, F. Liu, J. DeFazio, C. W. Narvaez Villarrubia, D. Finkenstadt, A. Shabaev, K. L. Jensen, V. Pavlenko, M. Mehl, S. Lambrakos, G. Gupta, A. D. Mohite, and N. A. Moody, *npj 2D Mater. Appl.* **1**, 12 (2017).
- ⁴N. A. Moody, K. L. Jensen, A. Shabaev, S. G. Lambrakos, J. Smedley, D. Finkenstadt, J. M. Pietryga, P. M. Anisimov, V. Pavlenko, E. R. Batista, J. W. Lewellen, F. Liu, G. Gupta, A. Mohite, H. Yamaguchi, M. A. Hoffbauer, and I. Robel, *Phys. Rev. Appl.* **10**, 047002 (2018).
- ⁵K. L. Jensen, D. Finkenstadt, D. A. Shiffler, A. Shabaev, S. G. Lambrakos, N. A. Moody, and J. J. Petillo, *J. Appl. Phys.* **123**, 065301 (2018).
- ⁶P. Zhang, *Sci. Rep.* **5**, 9826 (2015).
- ⁷L. F. Velasquez-Garcia and A. L. Akinwande, *Nanotechnology* **19**, 405305 (2008).
- ⁸S. Guerrero, L. Velasquez-Garcia, and A. Akinwande, *IEEE Trans. Electron Devices* **59**, 2524 (2012).
- ⁹L. Britnell, R. V. Gorbachev, R. Jalil, B. D. Belle, F. Schedin, A. Mishchenko, T. Georgiou, M. I. Katsnelson, L. Eaves, S. V. Morozov, N. M. R. Peres, J. Leist, A. K. Geim, K. S. Novoselov, and L. A. Ponomarenko, *Science* **335**, 947 (2012).
- ¹⁰J.-W. Han, J. S. Oh, and M. Meyyappan, *Appl. Phys. Lett.* **100**, 213505 (2012).

- ¹¹J.-W. Han, D.-I. Moon, and M. Meyyappan, *Nano Lett.* **17**, 2146 (2017).
- ¹²M. C. Meyyappan, in *EPS Heterogeneous Integration Roadmap*, edited by P. Wesling (IEEE, 2019), pp. 16.1–16.42.
- ¹³P. Hommelhoff, Y. Sortais, A. Aghajani-Talesh, and M. A. Kasevich, *Phys. Rev. Lett.* **96**, 077401 (2006).
- ¹⁴C. Ropers, D. Solli, C. Schulz, C. Lienau, and T. Elsaesser, *Phys. Rev. Lett.* **98**, 043907 (2007).
- ¹⁵J. R. Harris, *IEEE Trans. Plasma Sci.* **46**, 1872 (2018).
- ¹⁶H. Padamsee and J. Knobloch, *AIP Conf. Proc.* **474**(1), 212–248 (1999).
- ¹⁷P. Rumbach and D. B. Go, *J. Appl. Phys.* **112**, 103302 (2012).
- ¹⁸D. B. Go, *J. Phys. D: Appl. Phys.* **46**, 035202 (2013).
- ¹⁹X. Tan, P. Rumbach, N. Griggs, K. L. Jensen, and D. B. Go, *J. Appl. Phys.* **120**, 213301 (2016).
- ²⁰D. Shiffler, S. Fairchild, W. Tang, B. Maruyama, K. Golby, M. LaCour, M. Pasquali, and N. Lockwood, *IEEE Trans. Plasma Sci.* **40**, 1871 (2012).
- ²¹W. Tang, K. Golby, M. LaCour, and T. Knowles, *IEEE Trans. Plasma Sci.* **42**, 2580 (2014).
- ²²W. W. Tang, D. A. Shiffler, J. R. Harris, K. L. Jensen, K. Golby, M. LaCour, and T. Knowles, *AIP Adv.* **6**, 095007 (2016).
- ²³S. Karkare, D. Dimitrov, W. Schaff, L. Cultrera, A. Bartnik, X. Liu, E. Sawyer, T. Esposito, and I. V. Bazarov, *J. Appl. Phys.* **113**, 104904 (2013).
- ²⁴D. A. Dimitrov, R. Bushy, D. L. Bruhwiler, J. R. Cary, I. Ben-Zvi, T. Rao, X. Chang, J. Smedley, and Q. Wu, in *Proceedings of the IEEE Particle Accelerator Conference* (IEEE, 2007), p. THPAS020.
- ²⁵Y. Ang, S.-J. Liang, and L. Ang, *MRS Bull.* **42**, 505 (2017).
- ²⁶L. K. Ang, W. S. Koh, Y. Y. Lau, and T. J. T. Kwan, *Phys. Plasmas* **13**, 056701 (2006).
- ²⁷K. L. Jensen, D. A. Shiffler, M. Peckerar, J. R. Harris, and J. J. Petillo, *J. Appl. Phys.* **122**, 064501 (2017).
- ²⁸X. Wang and P. Musumeci, *Future of Electron Sources: Report of the Basic Energy Sciences Workshop on the Future of Electron Sources* (U.S. Department of Energy Office of Science, 2016).
- ²⁹A. Neukirch, S. Lewis, F. Liu, W. Nie, N. Moody, A. Mohite, and S. Tretiak, *Abstr. Pap. Am. Chem. Soc.* **257**, 476 (2019).
- ³⁰A. J. Neukirch, W. Nie, J.-C. Blancon, K. Appavoo, H. Tsai, M. Y. Sfeir, C. Katan, L. Pedesseau, J. Even, J. J. Crochet, G. Gupta, A. D. Mohite, and S. Tretiak, *Nano Lett.* **16**, 3809 (2016).
- ³¹J. J. Petillo, E. Nelson, J. Deford, N. Dionne, and B. Levush, *IEEE Trans. Electron Devices* **52**, 742 (2005).
- ³²J. Petillo, K. Eppley, D. Panagos, P. Blanchard, E. Nelson, N. Dionne, J. DeFord, B. Held, L. Chernyakova, W. Krueger, S. Humphries, T. McClure, A. Mondelli, J. Burdette, M. Cattellino, R. True, K. Nguyen, and B. Levush, *IEEE Trans. Plasma Sci.* **30**, 1238 (2002).
- ³³D. Dimitrov, R. Busby, J. Cary, I. Ben-Zvi, T. Rao, J. Smedley, X. Chang, J. Keister, Q. Wu, and E. Muller, *J. Appl. Phys.* **108**, 073712 (2010).
- ³⁴J. Browning and J. Watrous, *J. Vac. Sci. Technol. B* **29**, 02B109 (2011).
- ³⁵D. A. Dimitrov, G. I. Bell, J. Smedley, I. Ben-Zvi, J. Feng, S. Karkare, and H. A. Padmore, *J. Appl. Phys.* **122**, 165303 (2017).
- ³⁶P. Zhang, A. Valfells, L. K. Ang, J. W. Luginsland, and Y. Y. Lau, *Appl. Phys. Rev.* **4**, 011304 (2017).
- ³⁷R. Kishek, S. Bernal, C. Bohn, D. Grote, I. Haber, H. Li, P. G. O'Shea, M. Reiser, and M. Walter, *Phys. Plasmas* **10**, 2016 (2003).
- ³⁸D. Chernin, Y. Y. Lau, J. J. Petillo, S. Ovtchinnikov, D. Chen, A. Jassem, R. Jacobs, D. Morgan, and J. H. Booske, *IEEE Trans. Plasma Sci.* **48**, 146 (2020).
- ³⁹Y. Y. Lau, *J. Appl. Phys.* **61**, 36 (1987).
- ⁴⁰W. Li and D. Y. Li, *J. Chem. Phys.* **122**, 064708 (2005).
- ⁴¹D. Dowell, I. Bazarov, B. Dunham, K. Harkay, C. Hernandez-Garcia, R. Legg, H. Padmore, T. Rao, J. Smedley, and W. Wan, *Nucl. Instrum. Methods Phys. Res. Sect. A* **622**, 685 (2010).
- ⁴²E. Merzbacher, *Phys. Today* **55**(8), 44 (2002).
- ⁴³G. Gamow, *Nature* **122**, 805 (1928).
- ⁴⁴R. W. Gurney and E. U. Condon, *Nature* **122**, 439 (1928).
- ⁴⁵R. W. Gurney and E. U. Condon, *Phys. Rev.* **33**, 127 (1929).
- ⁴⁶J. R. Oppenheimer, *Phys. Rev.* **31**, 66 (1928).
- ⁴⁷R. H. Fowler and L. Nordheim, *Proc. R. Soc. Lond. A* **119**, 173 (1928).
- ⁴⁸R. A. Millikan and C. F. Eyring, *Phys. Rev.* **27**, 51 (1926).
- ⁴⁹R. H. Fowler, *Proc. R. Soc. Lond. A* **117**, 549 (1928).
- ⁵⁰R. H. Fowler, *Proc. R. Soc. A* **118**, 229 (1928).
- ⁵¹K. L. Jensen, *IEEE Trans. Plasma Sci.* **46**, 1881 (2018).
- ⁵²C. Herring and M. Nichols, *Rev. Mod. Phys.* **21**, 185 (1949).
- ⁵³C. Crowell, *Solid-State Electron.* **8**, 395 (1965).
- ⁵⁴E. Rhoderick, *J. Phys. D: Appl. Phys.* **3**, 1153 (1970).
- ⁵⁵E. Rhoderick, *IEE Proc. I Solid-State Electron Dev.* **129**, 1 (1982).
- ⁵⁶R. E. Hummel, *Electronic Properties of Materials* (Springer-Verlag, Berlin, 1992).
- ⁵⁷C. J. Edcombe, in *Advances in Imaging and Electron Physics*, Vol. 162, edited by P. Hawkes (Elsevier, 2010) pp. 77–127.
- ⁵⁸W. W. Lui and M. Fukuma, *J. Appl. Phys.* **60**, 1555 (1986).
- ⁵⁹K. Brennan and C. Summers, *J. Appl. Phys.* **61**, 614 (1987).
- ⁶⁰K. L. Jensen and A. Ganguly, *J. Appl. Phys.* **73**, 4409 (1993).
- ⁶¹K. L. Jensen, *Introduction to the Physics of Electron Emission* (John Wiley & Sons, Inc., Hoboken, NJ, 2017).
- ⁶²Y. Y. Lau, D. Chernin, D. Colombant, and P. Ho, *Phys. Rev. Lett.* **66**, 1446 (1991).
- ⁶³S. Banerjee and P. Zhang, *AIP Adv.* **9**, 085302 (2019).
- ⁶⁴J. Sune, P. Olivo, and B. Ricco, *J. Appl. Phys.* **70**, 337 (1991).
- ⁶⁵J. Sune, P. Olivo, and B. Ricco, *IEEE Trans. Electron Devices* **39**, 1732 (1992).
- ⁶⁶R. Waters and B. Van Zeghbroeck, *Appl. Phys. Lett.* **73**, 3692 (1998).
- ⁶⁷R. Waters and B. Van Zeghbroeck, *Appl. Phys. Lett.* **75**, 2410 (1999).
- ⁶⁸A. Gehring and A. Selberherr, in *Handbook of Theoretical and Computational Nanotechnology*, edited by M. Rieth and W. Schommers (American Scientific Publishers, Stevenson Ranch, CA, 2006), pp. 469–543.
- ⁶⁹L. Brillson, *Surf. Sci.* **299–300**, 909 (1994).
- ⁷⁰W. Mönch, *Semiconductor Surfaces and Interfaces*, Springer Series in Surface Sciences Vol. 26 (Springer-Verlag, New York, 1995).
- ⁷¹B. Jonker, *Proc. IEEE* **91**, 727 (2003).
- ⁷²S. M. Sze and K. K. Ng, *Physics of Semiconductor Devices* (Wiley-Interscience, Hoboken, NJ, 2007), x, 815 pp.
- ⁷³L. J. Brillson, *Surfaces and Interfaces of Electronic Materials* (Wiley-VCH, Weinheim, 2010).
- ⁷⁴L. J. Brillson and Y. Lu, *J. Appl. Phys.* **109**, 121301 (2011).
- ⁷⁵J. Zuber, K. L. Jensen, and T. Sullivan, *J. Appl. Phys.* **91**, 9379 (2002).
- ⁷⁶C. Edcombe and U. Valdre, *Philos. Mag. B* **82**, 987 (2002).
- ⁷⁷D. Jaeger, J. Hren, and V. Zhirmov, *J. Appl. Phys.* **93**, 691 (2003).
- ⁷⁸R. G. Forbes, C. Edcombe, and U. Valdre, *Ultramicroscopy* **95**, 57 (2003).
- ⁷⁹K. L. Jensen, D. W. Feldman, and P. G. O'Shea, *J. Vac. Sci. Technol. B* **23**, 621 (2005).
- ⁸⁰G. Kokkorakis, A. Modinos, and J. Xanthakis, *J. Appl. Phys.* **91**, 4580 (2002).
- ⁸¹A. Kyritsakis, G. Kokkorakis, J. Xanthakis, T. Kirk, and D. Pescia, *Appl. Phys. Lett.* **97**, 023104 (2010).
- ⁸²A. Kyritsakis and J. P. Xanthakis, *J. Appl. Phys.* **119**, 045303 (2016).
- ⁸³M. Krüger, C. Lemell, G. Wachter, J. Burgdörfer, and P. Hommelhoff, *J. Phys. B: At. Mol. Opt. Phys.* **51**, 172001 (2018).
- ⁸⁴J. G. Simmons, *J. Appl. Phys.* **34**, 1793 (1963).
- ⁸⁵R. Stratton, *Proc. Phys. Soc. Sect. B* **68**, 746 (1955).
- ⁸⁶K. L. Jensen, *J. Appl. Phys.* **111**, 054916 (2012).
- ⁸⁷K. L. Jensen, *J. Appl. Phys.* **126**, 065302 (2019).
- ⁸⁸E. L. Murphy and R. H. Good, *Phys. Rev.* **102**, 1464 (1956).
- ⁸⁹K. L. Jensen, M. McDonald, J. R. Harris, D. A. Shiffler, M. Cahay, and J. J. Petillo, *J. Appl. Phys.* **126**, 245301 (2019).
- ⁹⁰R. G. Forbes and J. H. B. Deane, *Proc. R. Soc. Lond. A* **463**, 2907 (2007).
- ⁹¹P. Cutler and D. Nagy, *Surf. Sci.* **3**, 71 (1965).
- ⁹²N. Fröman and P. O. Fröman, *Int. J. Quantum Chem.* **35**, 751 (1989).
- ⁹³N. Lang and W. Kohn, *Phys. Rev. B* **7**, 3541 (1973).
- ⁹⁴A. Evtukh, H. Hartnagel, O. Yilmazoglu, H. Mimura, and D. Pavlidis, *Vacuum Nanoelectronic Devices* (John Wiley & Sons, 2015).

- ⁹⁵R. Tsu and L. Esaki, *Appl. Phys. Lett.* **22**, 562 (1973).
- ⁹⁶L. Esaki, *Rev. Mod. Phys.* **46**, 237 (1974).
- ⁹⁷E. Kemble, *Phys. Rev.* **48**, 549 (1935).
- ⁹⁸K. L. Jensen, in *Modern Developments in Vacuum Electron Sources*, edited by G. Gaertner, W. Knapp, and R. Forbes (Springer, 2020).
- ⁹⁹W. W. Dolan and W. P. Dyke, *Phys. Rev.* **95**, 327 (1954).
- ¹⁰⁰A. E. Bell and L. W. Swanson, *Phys. Rev. B* **19**, 3353 (1979).
- ¹⁰¹J. W. Gadzuk and E. W. Plummer, *Phys. Rev. B* **3**, 2125 (1971).
- ¹⁰²H. Mimura, H. Shimawaki, and K. Yokoo, *Electron. Commun. Jpn.* **84**, 1 (2001).
- ¹⁰³S. Yakunin, M. Sytnyk, D. Kriegner, S. Shrestha, M. Richter, G. J. Matt, H. Azimi, C. J. Brabec, J. Stangl, M. V. Kovalenko, and W. Heiss, *Nat. Photon.* **9**, 444 (2015).
- ¹⁰⁴K. L. Jensen, D. Finkenstadt, A. Shabaev, S. G. Lambrakos, N. A. Moody, J. J. Petillo, H. Yamaguchi, and F. Liu, *J. Appl. Phys.* **123**, 045301 (2018).
- ¹⁰⁵A. Hiraiwa, T. Saito, A. Daicho, and H. Kawarada, *J. Appl. Phys.* **114**, 134501 (2013).
- ¹⁰⁶J. Robertson, *J. Vac. Sci. Technol. B* **17**, 659 (1999).
- ¹⁰⁷P. Lerner, P. H. Cutler, and N. Miskovsky, *J. Vac. Sci. Technol. B* **15**, 337 (1997).
- ¹⁰⁸H. Mimura, Y. Abe, J. Ikeda, K. Tahara, Y. Neo, H. Shimawaki, and K. Yokoo, *J. Vac. Sci. Technol. B* **16**, 803 (1998).
- ¹⁰⁹J. A. Lopez-Villanueva, J. A. Jimenez-Tejada, P. Cartujo, J. Bausells, and J. E. Carceller, *J. Appl. Phys.* **70**, 3712 (1991).
- ¹¹⁰M. Lenzlinger and E. H. Snow, *J. Appl. Phys.* **40**, 278 (1969).
- ¹¹¹J. H. B. Deane and R. G. Forbes, *J. Phys. A: Math. Theor.* **41**, 395301 (2008).